

Installation and commissioning of the monitor spectrometer of KATRIN

Diplomarbeit
vorgelegt
von

Johannes David Goullon

Am Institut für Experimentelle Kernphysik (IEKP)
Karlsruher Institut für Technologie (KIT)

Erstgutachter: Prof. Dr. Guido Drexlin
Zweitgutachter: Prof. Dr. Thomas Müller

Bearbeitungszeit: 15. November 2009 – 15. November 2010

Erklärung

Hiermit versichere ich, die vorliegende Arbeit selbständig angefertigt, alle dem Wortlaut oder Sinn nach entnommenen Inhalte anderer Werke an den entsprechenden Stellen unter Angabe der Quellen kenntlich gemacht und keine weiteren Hilfsmittel verwendet zu haben.

Johannes Goullon
Karlsruhe, November 2010

Zusammenfassung

Das **K**arlsruher **T**ritium **N**eutrino (KATRIN) Experiment hat das Ziel, die Neutrinomasse mit einer Sensitivität von $0,2\text{ eV}$ (90% C.L.) zu bestimmen. Dazu vermisst KATRIN den Endpunkt des Tritium- β -Spektrums mit Hilfe des für die Präzisions- β -Spektroskopie besonders geeigneten MAC-E-Filter Prinzips. Dieses Prinzip lässt die Spektrometer als integrierende Hochpassfilter wirken und wandelt die transversale Energie der Elektronen mittels adiabatischer Magnetfeldänderung in longitudinale Energie um.

Um die Designsensitivität zu erreichen, muss die Summe aller systematischen Unsicherheiten kleiner als $0,017\text{ eV}^2$ sein. Dementsprechend dürfen die einzelnen Quellen für die systematische Unsicherheit von KATRIN nur im 10^{-3} eV^2 Bereich beitragen. Ein wesentlicher Beitrag zu systematischen Fehlerquellen sind unbemerkte Variationen in der Hochspannung, die zum Abscannen des β -Spektrums verwendet wird. Diese intrinsischen HV-Fluktuationen müssen kleiner als 3 ppm sein, was bei einer Spannung von $18,6\text{ kV}$ einer maximalen Änderung von $\pm 60\text{ mV}$ entspricht. Um die Hochspannung derart genau zu überwachen wurden zwei Konzepte entwickelt, die in den späteren Messungen parallel benutzt werden: Erstens wurden zwei hochpräzise Spannungsteiler im ppm-Stabilitätsbereich gebaut, die die Hochspannung in den Niederspannungsbereich bis 10 V herunterteilen, die dann mit Präzisionsvoltmetern gemessen wird. Zweitens wurde ein zweites Strahlführungssystem mit einem weiteren Retardierungsspektrometer (das Monitorspektrometer) gebaut, das an derselben Hochspannung wie die eigentliche KATRIN Strahlachse angeschlossen ist. Es vermisst eine monoenergetische Elektronenlinie nahe dem Tritiumendpunkt. Eine Verschiebung dieser Linie impliziert daher eine Änderung des aktuellen Retardierungspotentials.

Im Rahmen der Diplomarbeit wurde dieses Monitorspektrometer aufgebaut und in Betrieb genommen. Nachfolgend werden die einzelnen Kapitel dieser Arbeit zusammengefasst, Zitate und genauere Erläuterungen sind dem englischen Haupttext zu entnehmen.

1. **Einleitung** Neutrinos sind wichtige Schlüsselteilchen der heutigen Astroteilchen Physik. Durch ihre geringe Wechselwirkung mit Materie wurde ihre Existenz erst 1956 nachgewiesen, d.h. mehr als zwanzig Jahre nach ihrem Postulat durch W. Pauli. Heute sind Neutrinos als integraler Bestandteil des Standard Modells aufgenommen - doch ihre masselose Beschreibung erwies sich als nicht

korrekt, als 1998 Neutrinooszillationen nachgewiesen wurden. Diese setzen eine nichtverschwindende Masse für Neutrinos voraus, was auf Physik jenseits des Standard Modells hindeutet. Auch die Verletzung der Leptonenfamilienzahl weist auf eine notwendige Erweiterung des Standard Modells hin. Durch Neutrinooszillationen können aber nur Massendifferenzen und Mischungswinkel bestimmt werden, die Bestimmung der absoluten Masse muss durch sogenannte direkte oder indirekte Methoden erfolgen. Dabei sind die indirekten Methoden wie z. B. der neutrinolose doppelte β Zerfall ($0\nu\beta\beta$) modellabhängig, während die direkten Methoden wie Flugzeitbetrachtungen bei Supernovae und kinematische Untersuchungen modellunabhängig sind. Die bisher niedrigsten Obergrenzen für die Neutrinomasse lieferten die Tritium Zerfalls Experimente in Mainz und Troitsk mit $m(\nu) < 2.3 \text{ eV}$ (95 %), die nach demselben Prinzip wie KATRIN funktionieren.

2. **Das KATRIN - Experiment** Die bisherigen Experimente zur Bestimmung der absoluten Neutrinomasse sind durch die statistischen und systematischen Fehler limitiert auf einen Sensitivitätsbereich von ca. 2 eV. KATRIN hat das Ziel eine Sensitivität von 0,2 eV zu erreichen, was signifikante Verbesserungen im Hinblick auf die Statistik und die Systematik erfordert.

Das KATRIN Experiment untersucht hierzu den Endpunkt des Tritium- β -Spektrums mit bisher unerreichter Präzision, da nur dieser enge Bereich von der Neutrinomasse beeinflusst wird. Das Grundprinzip ist der MAC-E-Filter. Bei diesem werden die Elektronen adiabatisch in der Quelle durch starke Magnetfelder geführt und durch eine Magnetfeldänderung um vier Größenordnungen wird ihre transversale Energie fast vollständig in die longitudinale Komponente umgewandelt. Ein elektrostatisches Potential filtert die Elektronen: Es gelangen nur diejenigen β -Elektronen zum Detektor, deren Energie ausreicht, um den Potentialwall zu überwinden.

Der gesamte Aufbau von KATRIN besteht aus der fensterlosen gasförmigen Tritiumquelle, einer differentiellen und kryogenen Pumpstrecke, dem Vor- und Hauptspektrometer und dem Detektor. In der Tritiumquelle zerfällt molekulares Tritium (T_2) und wird durch einen geschlossenen Tritiumkreislauf gereinigt und wieder in die Quelle injiziert. Die darauffolgenden Pumpstrecken verringern die Gasdichte und damit die Tritiumdichte um 14 Größenordnungen. Mit dem daran anschließenden Vorspektrometer können niederenergetische Elektronen vorgefiltert werden, da diese keine Information über die Neutrinomasse tragen. Außerdem dient es als effektive Tritium-Pumpe vor dem Hauptspektrometer, das die verbleibenden hochenergetischen Elektronen mit einer Energieauflösung von $\Delta E = 0.93 \text{ eV}$ analysiert. Eine zweite Strahlachse mit einem dritten MAC-E-Filter überwacht die Variation in der Hochspannung durch Vermessung einer monoenergetischen Elektronenlinie.

3. **Das Monitorspektrometer** dient der Hochspannungsüberwachung des KATRIN Experiments. Dazu wurde im Rahmen dieser Arbeit das Spektrometer des früheren Mainzer Neutrinomassenexperiments für diesen Zweck umgebaut. Das Vakuumsystem ist komplett überarbeitet worden, das Luftspulensystem EMCS¹ zur Erdmagnetfeldkompensation wurde neu aufgebaut. Im Rahmen

¹Earth Magnetic Field Compensation System

dieser Arbeit wurden diese neuen und die alten Systeme, d.h. das Ultra-hochvakuum-System, das Heizsystem, das Hochspannungssystem, die Solenoide und die Luftspulen aufgebaut und in Betrieb genommen. Der Quellenhalter und die Quellkammer wurden modifiziert. Als Quelle dient beim Monitorspektrometer nach Tests verschiedener Elemente eine Festkörperquelle, in der ^{83}Rb ($T_{1/2} = 86.2 d$) in das kurzlebige β -emittierende Isotop $^{83\text{m}}\text{Kr}$ ($T_{1/2} = 1.83 h$) zerfällt. $^{83\text{m}}\text{Kr}$ liegt mit einer Elektronenenergie von 17,824 keV nahe genug am Tritiumendpunkt mit 18,6 keV, um zur kontinuierlichen Hochspannungsüberwachung benutzt zu werden. Wegen der geringen intrinsischen Breite (FWHM) der K_{32} Konversionselektronenlinie von 2,8 eV wurde die Energieauflösung des Monitorspektrometers an die des Hauptspektrometers von 0,93 eV angepasst. Eine dieser Quellen wurde im Rahmen dieser Diplomarbeit hergestellt. Da der Detektor erst in den letzten Wochen dieser Arbeit fertiggestellt wurde, konnte er entgegen den ursprünglichen Planungen des Gesamtsystems nicht mehr in Betrieb genommen werden. Das System ist aber zum jetzigen Zeitpunkt komplettiert und voll einsatzfähig.

Parallel zu den Hardwareaufgaben umfasste diese Arbeit auch wesentliche Softwareaufgaben: Die Software für die spätere Datenanalyse wurde neu programmiert.

4. **Das Luftspulensystem** des Monitorspektrometers besteht (in enger Analogie zum System beim Hauptspektrometer) aus zwei Systemen: dem EMCS (**E**arth **M**agnetic **F**ield **C**ompensation **S**ystem) und dem LFCS (**L**ow **F**ield **C**ompensation **S**ystem). Im Rahmen dieser Arbeit wurden diese Systeme aufgebaut und es wurden detaillierte Messungen durchgeführt, um die Ströme zu ermitteln, die im Betrieb genutzt werden sollen. Die Erdmagnetfeldkompensation mit dem EMCS funktioniert zuverlässig - das Magnetfeld wurde in der Analysierebene des Monitorspektrometers von $40 \mu\text{T}$ auf wenige μT kompensiert. Beim LFCS wurden die drei Stromkreise der Spulen separat betrieben und mit Berechnungen nach Biot-Savart verglichen, damit ergab sich eine hinreichend gute Übereinstimmung.

Beim Betrieb der beiden Systeme wich die Messung bei den Komponenten senkrecht zur Spektrometerachse signifikant von den Erwartungen ab (sie sollten ca. $0 \mu\text{T}$ betragen, waren aber bis zu $10 \mu\text{T}$ groß). Daher wurde eine detaillierte Simulation durchgeführt. Diese bestätigte die Vermutung, dass eine geringe Verkipfung der Messstange mit der Hallsonde der Grund für diese Abweichungen war.

Zusammenfassend lässt sich sagen, dass die Luftspulensysteme des Monitorspektrometers funktionieren und das gesamte Spektrometersystem nun einsatzbereit sind.

Contents

1. Introduction	1
1.1. Neutrino oscillations	1
1.1.1. Basic theoretical principles	2
1.1.2. Evidence of neutrino oscillations at different neutrinosources	2
1.2. Neutrinos in cosmology and particle physics	6
1.3. Determination of the neutrino mass	8
1.3.1. β decay	8
1.3.2. Neutrino mass determination from π and τ decays	10
1.3.3. Neutrinoless double β decay	10
1.3.4. Time-of-flight determination of supernovae neutrinos	11
1.3.5. Cosmological determination	11
2. The KATRIN experiment	13
2.1. MAC-E-Filter	13
2.1.1. Transmission function	15
2.2. Experimental setup	16
2.2.1. The windowless gaseous Tritium source (WGTS) and the rear section	16
2.2.2. Pumping section	17
2.2.3. Pre- and main spectrometer	17
2.2.4. Focal plane detector	17
2.2.5. High voltage monitoring	18
3. The monitor spectrometer	21
3.1. The spectrometer	21
3.2. Vacuum system	23
3.2.1. Principle	23
3.2.2. Status and results	24
3.3. Heating system	25
3.4. High voltage	26
3.5. Magnetic System	26
3.6. Air coil system	26
3.7. The Source	27
3.7.1. The source part of the spectrometer	27
3.7.2. The different sources and their suitability	28
3.7.3. The $^{241}\text{Am}/\text{Co}$ Source	29
3.7.4. The $^{83}\text{Rb}/^{83\text{m}}\text{Kr}$ -Sources	30
3.7.4.1. Condensed $^{83}\text{Rb}/^{83\text{m}}\text{Kr}$ -Source (CKrS)	31
3.7.4.2. Solid state $^{83}\text{Rb}/^{83\text{m}}\text{Kr}$ -Source (SKrS)	32

3.7.5. Conclusion	34
3.8. Detector	34
3.9. Slow control and data acquisition	35
3.10. Data analysis	36
4. The air coil system	39
4.1. Magnetic field measurements	39
4.1.1. Background measurements	39
4.1.2. Background compensation	41
4.1.3. Magnetic field measurements with the LFCS	41
4.2. Comparison to magnetic field simulation	42
4.3. Conclusion	43
5. Conclusion and outlook	45
Appendix	47
A. The wire scanner	47
B. Radon measurements and simulations	50
B.1. Radon measurements in Mainz	51
B.2. Radon simulations	52
B.3. Conclusion	56
C. Detector commissioning	57
D. Measurement programme	59
Bibliography	63

1. Introduction

Neutrinos are an important part of astro-particle physics - especially in the last few years the role of neutrinos in this field of work has increased substantially due to many new observations. Postulated in 1930 by W. Pauli to explain the continuous energy spectrum of the β -decay [Pau30], neutrinos were first detected 22 years after their theoretical description by E. Fermi 1934 [Fer34]. This was achieved by Cowan and Reines by making use of the inverse β -decay of free protons to identify the electro-anti-neutrinos in 1956 [C⁺56]. The detection of the muon- [D⁺62] and the tau-neutrino [K⁺01] followed in 1962 and 2000.

Nowadays neutrinos are an established part of the Standard Model of particle physics. They are electric neutral leptons, so they only interact through the weak force. In the Standard Model, neutrinos are massless particles with definite helicity - so there should only exist left-handed neutrinos and right-handed anti-neutrinos.

In 1998 neutrino flavour oscillations were observed [SKC98]. These breakthrough measurements point to new physics beyond the Standard Model, because only neutrinos with a non-zero mass can oscillate. Also, in this case the lepton family number is not conserved and the helicity of neutrinos is invertable now.

This chapter will give an overview of the actual status of neutrino physics to provide the framework and basic motivation for the KATRIN experiment, which then will be described in the second chapter.

1.1. Neutrino oscillations

The electron, muon, and tau neutrinos are the three distinct *flavor eigenstates* $|\nu_\alpha\rangle$ of the neutrinos. These are thus compounds of three different *mass eigenstates* $|\nu_i\rangle$. As each mass eigenstate $|\nu_i\rangle$ develops with a different phase in time during propagation, the original flavor eigenstate is encountered only with a certain probability along its flightpath.

1.1.1. Basic theoretical principles

As described above, the flavor eigenstates can be described as a linear combination of the mass eigenstates with the unitary PMNS lepton mixing matrix $U_{\alpha i}$ (the greek letters stand for the three flavor eigenstates, the latin letters for the three mass eigenstates) transforming both sets of eigenstates:

$$|\nu_\alpha\rangle = \sum_i U_{\alpha i} |\nu_i\rangle \quad \text{with the inversion} \quad |\nu_i\rangle = \sum_\alpha U_{i\alpha}^\dagger |\nu_\alpha\rangle \quad (1.1)$$

To describe the evolution in time one makes use of the Schrödinger equation:

$$|\nu(t)\rangle = \sum_i U_{\alpha i} e^{-iE_i t} |\nu_i\rangle = \sum_{i,\beta} U_{\alpha i} U_{\beta,i}^* e^{-iE_i t} |\nu_\beta\rangle \quad (1.2)$$

where E_i is the energy of the mass eigenstate i and t denotes the time.

The transition probability is calculated with $P(\alpha \rightarrow \beta, t) = |\langle \nu_\beta | \nu(t) \rangle|^2$. If, for simplicity, only two neutrino flavours are considered, only one mass difference $\Delta m^2 = m_2^2 - m_1^2$ and one mixing angle θ need to be regarded. The transition probability of such a system is described by the following formula [Sch97]:

$$P(\nu_\alpha \rightarrow \nu_\beta) = \sin^2(2\theta) \cdot \sin^2\left(\frac{\Delta m^2}{4} \cdot \frac{L}{E}\right) \quad (1.3)$$

So oscillations can only occur if $\theta \neq 0$ and $\Delta m^2 \neq 0$. The most important experimental variable is the ratio L/E - thus one should know exactly the distance to the source L and the energy E of the neutrinos.

1.1.2. Evidence of neutrino oscillations at different neutrino sources

To determine both the distance and the energy of the neutrinos, a precise knowledge of the sources and the generation mechanism is required. Another important aspect is the absolute value of the flux of neutrinos, as they have only a very small cross section for interaction with matter. An overview of known neutrino sources is given in figure 1.1. In order to detect neutrinos, they are required to have rather high energies so that they are able to react with nucleons or electrons.

Below the most important neutrino sources and the associated experiments are presented.

Atmospheric neutrinos are generated through the interaction of cosmic rays with atomic nuclei (N) in the upper atmosphere of the earth. Primary cosmic rays consist predominantly out of hadrons (mostly protons) so the following reactions and subsequent decay chains are important ν -sources:

$$\begin{aligned} p + N &\rightarrow \pi^\pm, K^\pm \rightarrow \mu^\pm + \nu_\mu/\bar{\nu}_\mu \\ &\hookrightarrow e^\pm + \nu_e/\bar{\nu}_e + \nu_\mu/\bar{\nu}_\mu \end{aligned} \quad (1.4)$$

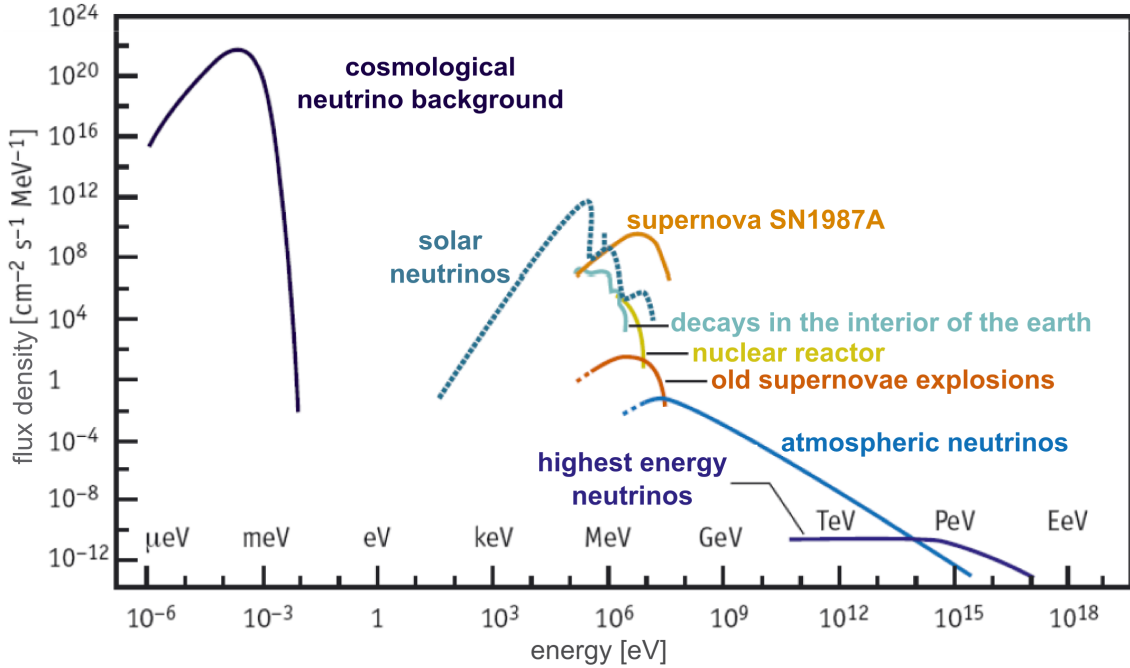


Figure 1.1.: Neutrino sources are shown here in a flux density-energy diagram. The detection of neutrinos requires high flux densities *and* high energies - therefore the cosmic neutrino background and the high-energetic neutrinos aren't suitable. Based on [Bru06]

As a result of the energy spectrum of primary cosmic rays extending over many orders of magnitude, the neutrino energies also differ from a few MeV up to 10^9 GeV. In 1998, the Super-Kamiokande experiment provided compelling evidence for oscillations of atmospheric neutrinos [SKC98]. Super-Kamiokande consists of a stainless steel tank filled with ultra-pure water. A large array of photomultipliers (PMTs) is installed on the tank walls to detect ν -interactions. When neutrinos cross the tank volume, they are able to generate charged leptons through charged current reactions (in this case muons and electrons are generated). These leptons then emit Cerenkov radiation, which is detected by the PMTs. This technique allows to measure both the energy and angle of the incoming neutrino. This in turn allows to differentiate between up- and downgoing neutrinos. Upgoing neutrinos cover a much bigger distance (about 13000 km through the earth) than downgoing ones (about 20 km through the atmosphere). Accordingly, these different L/E ratios (see formula 1.3) lead to detectable neutrino oscillations. As described in figure 1.2, Super-Kamiokande confirmed neutrino oscillations.

Their result was the following mass difference

$$1.9 \cdot 10^{-3} eV^2 < \Delta m_{atmos}^2 < 3.0 \cdot 10^{-3} eV^2 \quad (1.5)$$

and an angle which is close to the maximum mixing angle [SKC04]

$$\sin^2(2\theta_{atmos}) > 0.90 \quad (1.6)$$

both of them at 90% C.L.

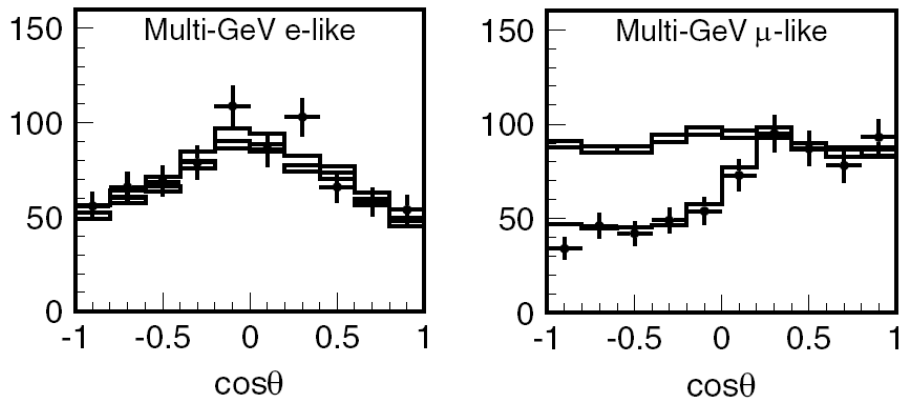


Figure 1.2.: Results of the Super-Kamiokande experiment The figures show the zenith-angle distribution (Number of events at different angles). The points show the data, the box histograms show the expected rate (Monte Carlo simulation), if neutrinos do not oscillate, while the lines show the best-fit oscillation expectations. The height of the boxes shows the statistical error of the Monte Carlo. The e-like events are consistent with the non-oscillated Monte Carlo, while the upgoing μ -like events differ clearly ($\cos(\theta) = -1$ corresponds to the longest distance). The line shows the best-fit expectation for oscillations with $\sin^2(2\theta) = 1.00$ and $\Delta m^2 = 2.1 \cdot 10^{-3} eV^2$. This provides clear evidence to $\nu_\mu \leftrightarrow \nu_\tau$ oscillations. The value of L/E is not suitable to observe oscillations of electron neutrinos. [SKC05]

Solar neutrinos The present **Standard Solar Model (SSM)** describes the nuclear fusion processes inside the sun, in which hydrogen is fused to helium:



In several subordinate processes electron-neutrinos with different fluxes and energies are generated (as seen in figure 1.1). In the 1970s the flux of the electron-neutrinos from the sun was measured for the first time [Dav55] and it was only one third of the prediction by the SSM. This discrepancy was known for a long time as the ‘solar neutrino problem’, which was finally solved in 2001 by the SNO experiment (‘Sudbury Neutrino Observatory’, [Col01]) and confirmed recently by Borexino in 2007 [A⁺08b]. The SNO experiment has a similar design as Super-Kamiokande, but uses heavy water (D_2O) as target. This heavy water measures not only the charged current on deuterium, but also the neutral one, which is sensitive to all neutrino flavors.

The SNO experiment in its charged current analysis also measured a too small flux of electron-neutrinos, but the bolometric flux of all neutrino flavors together is as large as predicted by the SSM. An explanation for this observation is given by the scenario, where electron-neutrinos change their flavor inside the sun via the MSW-effect [Wol78]. Accordingly, the SNO experiment published data [Col08] for the mass difference and for the mixing angle which is big but not maximal:

$$\Delta m_{solar}^2 = 4.57 \cdot 10^{-5} eV^2 \quad (1.8)$$

$$\tan^2(\theta_{solar}) = 0.447 \quad (1.9)$$

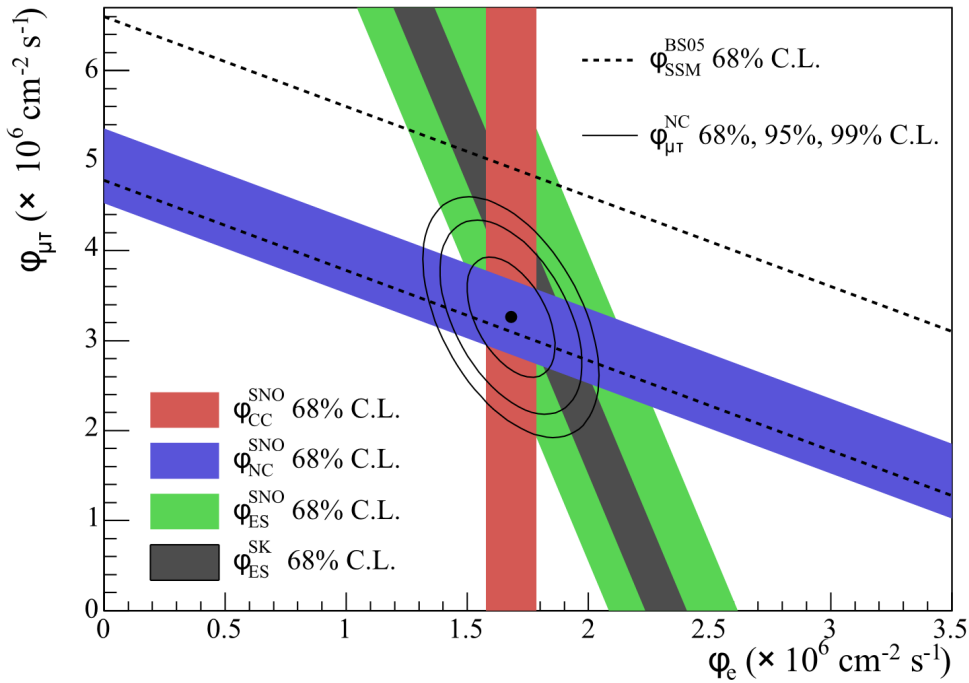


Figure 1.3.: Results from SNO and Super-Kamiokande experiments This chart shows the flux of muon- and tau-neutrinos over the electron-neutrino-flux. The prediction of the SSM for multi-flavor fluxes is indicated with the dashed lines. The red, blue and green bounds indicate the SNO results for the charged current (CC), the neutral current (NC) and the elastic scattering of electrons (ES) while the brown band shows the ES result from Superkamiokande. The oval lines are the best-fit values for the flux of μ - and τ -neutrinos. [SNO10]

Reactor neutrinos are generated in nuclear reactors by β^- decays of neutron-rich nuclides in the energy of a few MeV. The KamLAND experiment (“Kamioka Liquid scintillator Anti-Neutrino Detector”) is based on a liquid scintillator and analyzes the *disappearance*-channel of electron-anti-neutrinos from the surrounding nuclear power plants in Japan and Korea. KamLAND provided evidence for neutrino oscillations as well and supplied these values [Col05]:

$$\Delta m_{\text{react}}^2 = 7.9_{-0.5}^{+0.6} \cdot 10^{-5} \text{ eV}^2 \quad \tan^2(\theta_{\text{react}}) = 0.40_{-0.07}^{+0.10} \quad (1.10)$$

which are in good overall agreement with the solar values of equation 1.8 and 1.9. The most promising future reactor experiment is Double Chooz. This experiment will consist of two experimental sites, one in a distance of 400 m to the nuclear reactor and the other one in a distance of 1 km. With this setup it is possible to make a flux measurement of different L/E ratios and to go beyond the standard two-flavor oscillation investigations by targeting the final open parameter in ν -oscillations, the generic three-flavor parameter $\sin(\theta_{13})$.

Alltogether this framework of neutrino oscillations is supported by present experiments. Figure 1.4 gives an overview of measurement results of neutrino oscillations up to now.

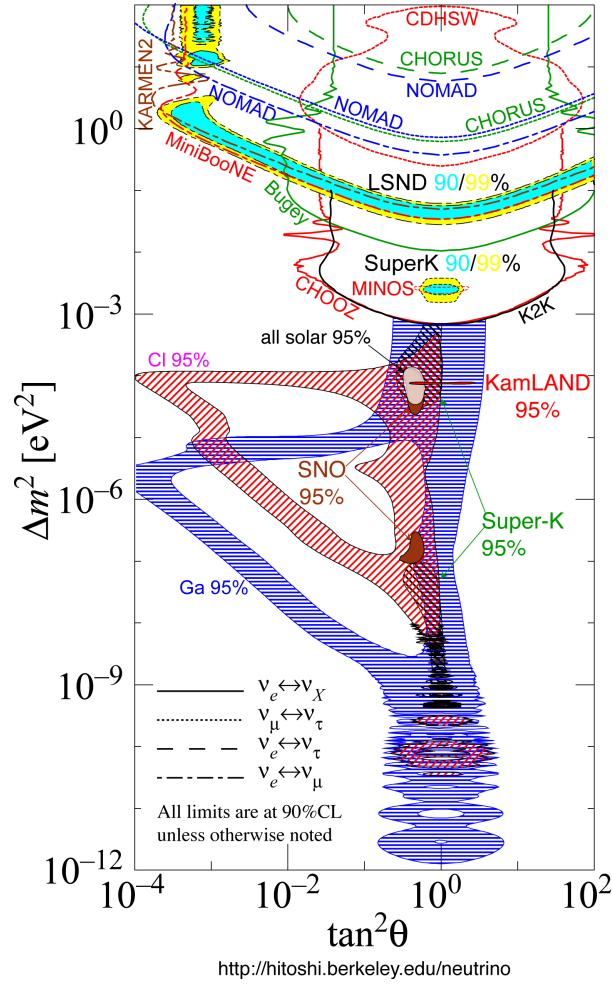


Figure 1.4.: Summary of measured oscillation parameters This figure shows the mass-differences Δm^2 over the mixing angles $\tan^2(\theta)$. The charts exclude the region above and to the right of the lines, while the colored areas mark the favored regions. The lines mark the searches for electron-neutrinos transforming into other neutrinos. The dotted lines indicate the $\nu_\mu \leftrightarrow \nu_\tau$ oscillations, the dashed lines indicate the $\nu_\tau \leftrightarrow \nu_e$ oscillations and the dot-dashed lines indicate the $\nu_\mu \leftrightarrow \nu_e$ oscillations. The SNO results in brown overlay with the ones from KamLAND and Super-Kamiokande and are generally accepted. The result from LSND is unconfirmed. [Mur10]

1.2. Neutrinos in cosmology and particle physics

The absolute neutrino mass value has a major implication for particle physics. In general, two generic mass scenarios can be figured out: the hierarchical (normal or inverted hierarchy) and the quasi-degenerated one (see figure 1.5). With the KATRIN experiment, which has a sensitivity in the sub-eV region, the quasi-degenerated scenario can be investigated and thus be confirmed or refused.

From the theoretical point of view, the origin of the mass of the neutrinos is also of major importance. It is not likely to be explained with the Higgs-mechanism, because the neutrino mass is several magnitudes smaller than the mass of any other elementary particle. A possible explanation is given by the Seesaw-model which has two types: in Seesaw I scenarios the small mass is due to a heavy right-handed Majorana neutrino. This theory prefers the hierarchic scenario observed in charged

leptons and quarks. The Seesaw type II model predicts a Higgs-Triplet which directly connects to the neutrino mass. This model prefers the quasi-degenerated scenario.

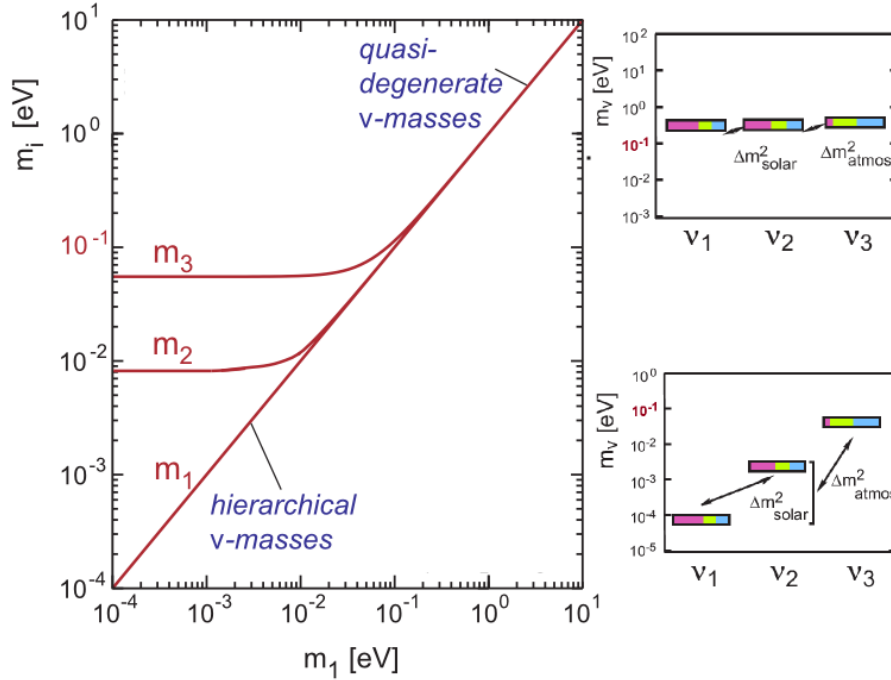


Figure 1.5.: Neutrino mass eigenstates m_i as a function of the lightest eigenstate m_1 . The quasi-degenerated scenario will result if the mass eigenstates m_i are much bigger than the mass differences Δm^2 . If the mass eigenstates m_i are roughly as big as the mass differences the hierarchical scenario will follow. The colors in the boxes illustrate the flavor fractions of the eigenstates. [KAT05]

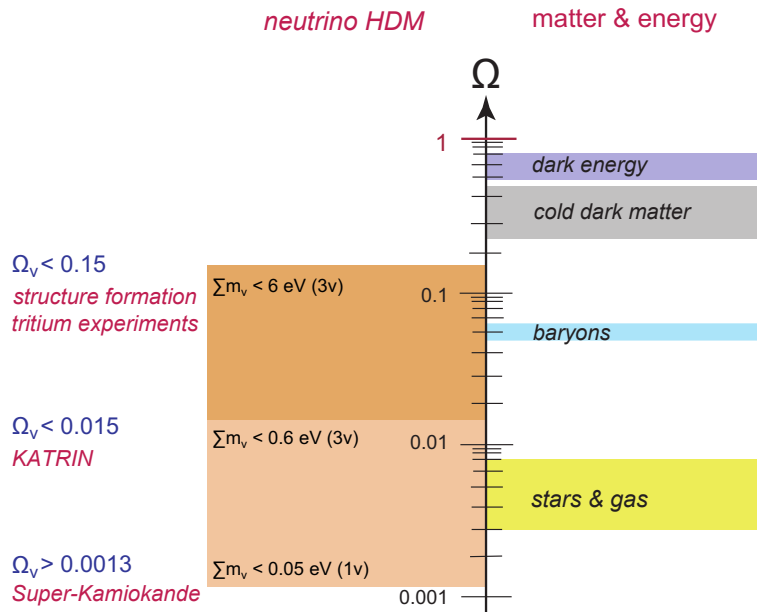


Figure 1.6.: Constituents of the energy density of the universe. On the right side the fraction of dark energy, dark matter, baryons and stars of the total energy density of the universe can be seen. On the left side the fraction of relic neutrino density is shown. The Hot Dark Matter content of the universe is constrained by experiments and cosmological theories. Based on [Thü07]

Neutrinos are also an important part of cosmological theories. Because of their large number of $336/\text{cm}^3$ in the present universe, which can be calculated by looking at their thermal distribution at the time of their decoupling, the neutrino mass can make a substantial contribution to the total energy density of the universe (see figure 1.6). An upper limit of 0.2 eV for the electron neutrino mass by KATRIN would clearly rule out any substantial contribution of primordial neutrinos, confining Hot Dark Matter to smaller than 1%.

As Hot Dark Matter, the neutrinos impact the structure formation of the universe, in addition to Cold Dark Matter both Dark Matter components lead to the structures that we are observing (galaxies, galaxy cluster and voids). If the neutrinos have a significant mass the matter distribution would be more homogeneous, because the relativistic free streaming of neutrinos tends to wash out large-scale structures.

The neutrino mass determination by the time-of-flight measurements of neutrinos from supernovae explosions is not as sensitive as with KATRIN. However, an absolute neutrino mass would advance our knowledge of the evolution of neutrino emission by supernovae significantly.

1.3. Determination of the neutrino mass

There are direct and indirect methods to determine the neutrino mass and some of them depend on models. Below several methods are explained and the associated experiments are presented.

1.3.1. β decay

β^- decay provides a stringent upper limit for the neutrino mass with the advantage of being model independent (it only depends on Fermi's theory of β -decay and energy-momentum conservation, both fact which are well proven).

These experiments determine the mass of the electron-anti-neutrino by measuring the continuous spectrum of the electrons resulting from the decay of a neutron inside a β -unstable nucleus:

$$n \rightarrow p + e^- + \bar{\nu}_e \quad (1.11)$$

Taking into account a non-zero neutrino mass, the electron spectrum is given by [KAT05]:

$$\frac{dN}{dE} = \frac{G_F^2}{2\pi^3} \cos^2 \theta_C |M|^2 \cdot F(Z, E) p(E + m_e c^2) (E_0 - E) \sqrt{(E_0 - E)^2 - m_\nu^2} \cdot \Theta(E_0 - E - m_\nu) \quad (1.12)$$

where E denotes the kinetic energy of the electron, m_e its mass and p its momentum. E_0 corresponds to the maximum electron energy (endpoint energy), $F(Z, E)$ is the Fermi function, G_F is the Fermi constant, θ_C is the Cabibbo angle and M is the nuclear matrix element. The Θ function assures that only real values are calculated. The neutrino mass parameter m_{ν_e} (the "electron neutrino mass") is the incoherent sum of the mass eigenstates:

$$m_{\nu_e}^2 = \sum_i |U_{ei}|^2 m_i^2 \quad (1.13)$$

It is important to note that the effect of the neutrino mass is only visible at the endpoint of the electron spectrum (see figure 1.7). In order to measure the spectrum

accurately close to the endpoint, a β -emitter with a very low energy is required. The β -emitter with the lowest endpoint energy is Rhenium with 2.47 keV, the second lowest energy is Tritium with 18.6 keV.

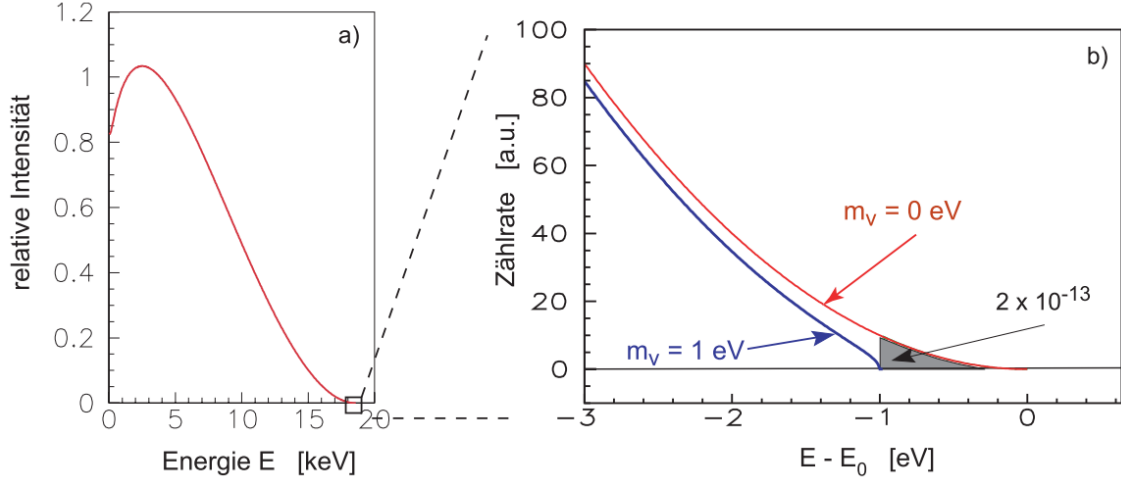


Figure 1.7.: Energy spectrum of electrons at the tritium-decay a) shows the whole energy spectrum. Only the part close to the endpoint is relevant for the neutrino mass (as seen in b)). $2 \cdot 10^{-13}$ of every electron from the tritium-decay has energies in this region. [KAT05]

Rhenium has the lowest endpoint energy. However, its major disadvantage is its very long half-life of $4.3 \cdot 10^{10}$ years. To obtain a sufficient counting rate a huge amount of rhenium is needed. Another disadvantage is the fact that the transition is forbidden - therefore formula 1.12 has to take account additional shape factors. An advantage of ^{187}Rh is that the source can be used simultaneously as detector. Bolometers consisting either of metallic rhenium or AgReO_4 and operated at milli Kelvin temperatures allow to detect the full energy of the released β electrons. A problem with this method is that every electron from the β -decay is measured and not only those close to the endpoint. Up to now this type of experiment sets an upper limit of the neutrino mass to [Col05]:

$$m_{\bar{\nu}_e} < 15 \text{ eV} \quad (1.14)$$

Future experiments like MARE will try to improve this upper limit.

Tritium has a larger endpoint energy but features a significantly smaller half-life of only 12.32 years. So much less tritium is needed to get the same rate as with rhenium. The tritium β -decay ${}^3\text{H} \rightarrow {}^3\text{He} + e^- + \bar{\nu}_e$ has some advantages for the calculation of the atomic corrections (simple electron shell configuration) and inelastic scattering (small atomic number). In comparison a disadvantage to rhenium are the final state effects: molecular tritium decays into excited states with a certain probability, so that some energy that is lost to the excited helium molecules, which might be interpreted as a neutrino mass if not properly taken into account.

Therefore equation 1.12 has to be modified to adjust it to the spectrum measured at KATRIN.

Present experiments use the MAC-E-Filter principle which is described in chapter 2.1. This MAC-E-Filter has the advantage that high energy electrons can be separated from the others. Up to now two experiments have determined upper limits for the neutrino mass: the Mainz experiment has yielded a limit of 2,3 eV (95% C.L.) [K⁺04], while the Troisk experiment reports a limit of 2.5 eV (95% C.L.) [L⁺99]. The combined result is the best upper limit today [A⁺08a]:

$$m_{\bar{\nu}_e} < 2,0 \text{ eV} \quad (1.15)$$

The KATRIN experiment will be able to improve the sensitivity for the neutrino mass down to $m_{\bar{\nu}_e} = 0.2 \text{ eV}$ with details being described in chapter 2.

1.3.2. Neutrino mass determination from π and τ decays

There is, in principle, also the possibility to determine upper limits of the ν_μ and ν_τ masses using kinematic methods. Here, the decays of pions ($\pi^\pm \rightarrow \mu^\pm + \nu_\mu/\bar{\nu}_\mu$) and tau ($\tau \rightarrow \pi^- \pi^- \pi^- \pi^+ \pi^+ (\pi^0) + \nu_\tau$) are analyzed. But these upper limits for the τ - and the μ -neutrino are significantly larger than the upper limit of the electron-anti-neutrino ($m_{\nu_\mu} < 190 \text{ keV}$ (90% C.L.) and $m_{\nu_\tau} < 18.2 \text{ MeV}$ (95% C.L.) [PDG10]).

1.3.3. Neutrinoless double β decay

A double β -decay ($2\nu\beta\beta$) process can occur when a single β -decay is energetically forbidden. It is only possible for nuclei with an even number of protons. This decay process proceeds via virtual states in a nucleus with an odd number of protons that is energetically higher. The final state is an energetically lower nucleus with an even number of protons. These processes have a very low probability; therefore $2\nu\beta\beta$ -decays have exceedingly long half-lives ($\approx 10^{20}$ years). By this decay two neutrons are converted into two protons and two electrons and two electron-anti-neutrinos are generated:

$$2n \rightarrow 2p + 2e^- + 2\bar{\nu}_e \quad (1.16)$$

For the neutrinoless double β -decay ($0\nu\beta\beta$) the neutrinos have to be Majorana particles (that means they are their own anti-particles), so this method is model dependant. The neutrino from the first β -decay has to induce the second one as a virtual exchange particle. In this case the spectrum is not continuous as it is in $2\nu\beta\beta$ -decay, but a monoenergetic line should appear when both electrons are detected simultaneously.

Up to now only a small team led by H. Klapdor-Kleingrothaus of the Heidelberg-Moscow experiment claims a positive signal from the decay of ^{76}Ge [KK⁺]. The final result was $m_{\nu_e} = (0.11 - 0.56) \text{ eV}$ (95% C.L.) but this finding is highly controversial because of the small statistical significance. Experiments like CUORE, EXO, GERDA, Xenon and MAJORANA will investigate the $0\nu\beta\beta$ -decay in the near future. The $0\nu\beta\beta$ decay is complementary to KATRIN, with the possibility that these experiments confirm each others results.

1.3.4. Time-of-flight determination of supernovae neutrinos

The neutrino mass can also be determined by analysing the time structure of supernovae neutrinos. The main drawback here is the fact that the emission spectrum of supernovae neutrinos has to be simulated. This spectrum has a certain width at the point of emission during the supernova explosion. For massless neutrinos this intrinsic width does not change on its way to earth, but for non-vanishing neutrino masses the arrival times will be modified: neutrinos with lower energies are slower than neutrinos with higher energies, so the latter should arrive first.

For Supernova SN1987A it was possible to investigate this energy-dependant time delay which resulted in an upper limit for the neutrino mass of 5.7 eV (95% C.L.) [A⁺08a].

1.3.5. Cosmological determination

The cosmological determination of the neutrino mass depends on the generic cosmological model (such as the Λ CDM model) and on the data sets used in the analysis. With these methods only an upper limit for the sum of all neutrino masses can be determined, because only the mass eigenstates influence the structure formation of the universe.

By making use of different combinations of the data sets various upper limits for the sum of the neutrino masses from 0.5 to 1.0 eV [Han05] have been established.

2. The KATRIN experiment

The **K**Arlsruhe **T**Ritium Neutrino experiment is a model-independent β -decay experiment that will constrain the neutrino mass with a sensitivity of 200 meV (90% C.L.). A potential neutrino mass of $m_{\nu_e} = 270$ meV can be determined with a statistical significance of 3σ .

This chapter will first present the basic measuring principle of KATRIN which is based on experiences gained at the experiments in Troitsk and Mainz, namely the MAC-E-Filter. Subsequently, the setup of KATRIN will be presented.

2.1. MAC-E-Filter

A MAC-E-Filter¹ is based on strong magnets providing a magnetic guiding field for β -electrons. Between the source and the detector magnet there is a minimum of the magnetic field. Furthermore there is an electrostatic potential that has its maximum at the minimum of the magnetic field. This plane is called the analyzing plane (see figure 2.1). The β -decay electrons are guided along the magnetic field lines along a cyclotron trajectory. Because of the small changes of the magnetic field along this trajectory the motion is adiabatic, so the product of the Lorentz factor and the magnetic moment of the cyclotron motion of the electrons is constant:

$$\gamma \cdot \mu = \text{const.} \quad \text{with} \quad \gamma = \frac{1}{\sqrt{1 - \left(\frac{v}{c}\right)^2}} \quad (2.1)$$

As the maximum Lorentz factor for tritium β -electrons is 1.04, equation 2.1 can be approximated:

$$\mu = \frac{E_{\perp}}{B} = \text{const.} \quad (2.2)$$

where E_{\perp} denotes the transversal electron energy and B the magnetic flux density.

¹Magnetic Adiabatic Collimation combined with an Electrostatic Filter

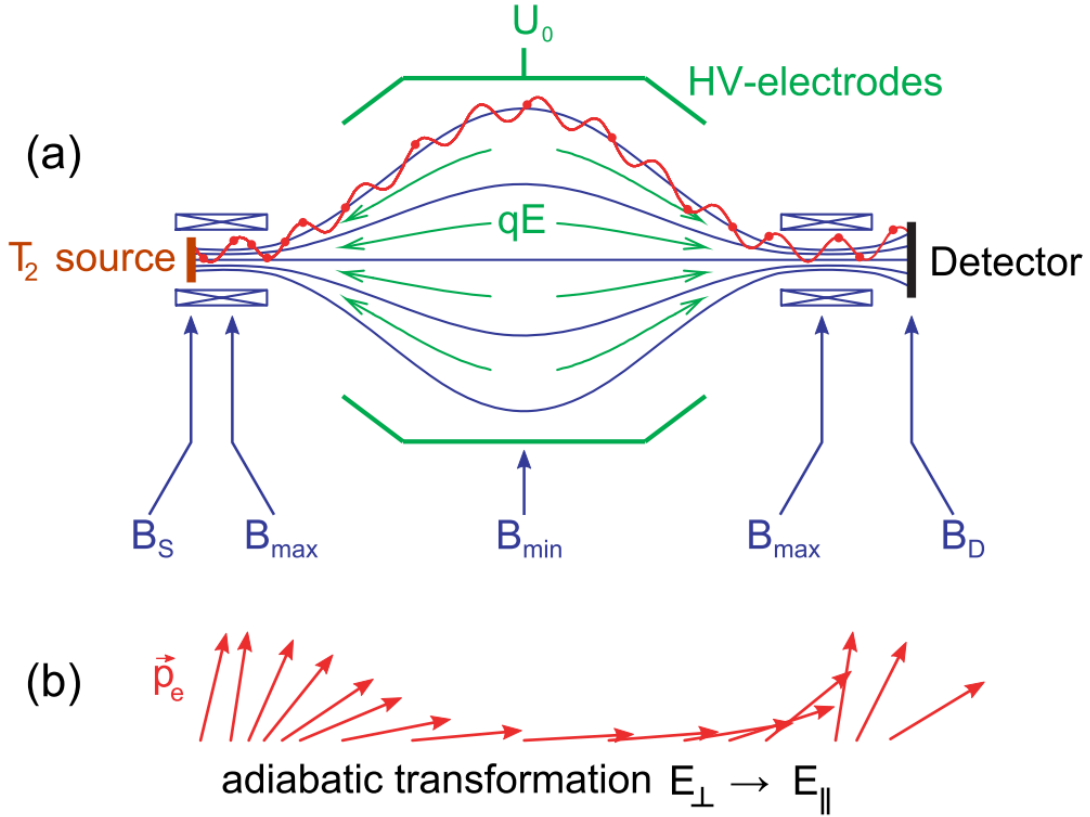


Figure 2.1.: Principle of the MAC-E-Filter a) The magnetic field is formed by two solenoids whose magnetic field (blue) gets smaller to the middle of the spectrometer and has its minimum at B_{min} in the analyzing plane. There the electric potential U (the electric force qE is plotted in green) has its maximum and gets smaller towards the outer parts of the spectrometer. Because of this electric potential only the electrons with an energy that exceeds the applied retarding voltage U_0 can pass. The red circular trajectory shows the path of the electrons as they move adiabatically on a cyclotron trajectory. b) Due to the fact that the magnetic field gets smaller in the analyzing plane, the transversal momentum is almost completely converted into the longitudinal momentum. [KAT05]

In the analyzing plane almost the entire kinetic energy of the electrons is directed longitudinally (figure 2.1b), so that electrons with a bigger energy than the electrostatic potential can cross the analyzing plane and reach the detector. The energy resolution ΔE thus depends only on the remaining transversal energy and results from formula 2.1:

$$\Delta E = \frac{B_{min}}{B_{max}} \cdot E = 0.93 \text{ eV} \quad (2.3)$$

with $B_{min} = 300 \text{ mT}$, $B_{max} = 6 \text{ T}$ and the endpoint energy of Tritium $E = 18600 \text{ eV}$.

Thus a MAC-E-Filter is an electrostatic highpass filter. The integrated spectrum is obtained by variation of the retarding potential.

This technique is unsurpassed in β -spectroscopy due to its good energy resolution for large fluxes allowing to make use of large-scale sources.

2.1.1. Transmission function

The transmission function is a very important parameter for the KATRIN experiment, as it describes which electrons starting at the source will pass the MAC-E-Filter and thus get transmitted to the detector. It is defined by the ratio of the electrons that start at the isotropic source to the ones that pass the retarding potential of the MAC-E-Filter.

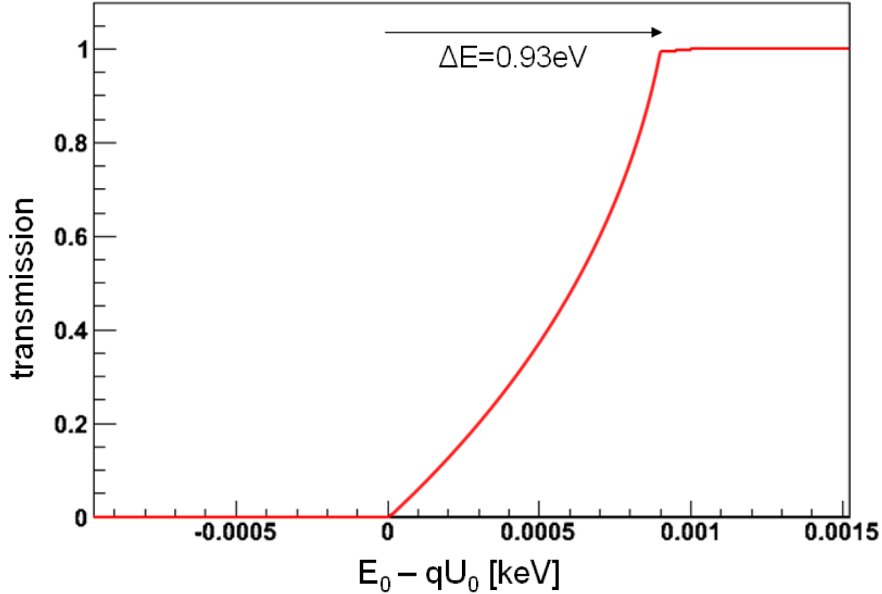


Figure 2.2.: Transmission function This is a typical shape of a transmission function for an isotropic electron source at KATRIN. Electrons with an energy below the retarding voltage cannot pass the MAC-E-Filter - the transmission is zero. Because of the finite energy resolution the function is not a step function but has a gradient with the width of the energy resolution ΔE . First the electrons with small starting angles are transmitted, at higher energies the electrons with higher starting angles can pass the MAC-E-Filter.

An electron that starts in the source at magnetic field B_{source} has two energy components of the total energy E_0 (θ is the starting angle of the electron between its momentum \vec{p} and the magnetic field \vec{B}): longitudinal $E_{\parallel} = E_0 \cdot \cos^2(\theta)$ and a transversal part $E_{\perp} = E_0 \cdot \sin^2(\theta)$. As the magnetic field μ decreases towards the analysing plane, E_{\perp} decreases too as the magnetic moment μ is constant (see equation 2.2). So the part of the energy $E_0 \cdot \sin^2(\theta) \cdot \frac{B_{source}}{B_{min}}$ cannot be analysed by the retarding energy $e \cdot U_0$.

If the source is not at the maximum magnetic field, some electrons are reflected.

This cut off angle is defined as: $\theta_{max} = \arcsin \sqrt{\frac{B_{source}}{B_{max}}}$.

The transmission function can now be derived (see [Frä10], [Bor00]):

$$\mathcal{T}(E_0, U_0) = \frac{\Delta\Omega}{2\pi} = 1 - \cos(\theta) = \begin{cases} 0 & \text{for } E_0 < eU_0 \\ \frac{1 - \sqrt{1 - \frac{E_0 - eU_0 \cdot \frac{B_{source}}{B_{min}}}}{E_0}}}{1 - \sqrt{1 - \frac{B_{source}}{B_{max}}}} & \text{for } eU_0 \leq E_0 \leq \frac{eU_0}{1 - \frac{B_{min}}{B_{max}}} \\ 1 & \text{for } \frac{eU_0}{1 - \frac{B_{min}}{B_{max}}} \leq E_0 \end{cases} \quad (2.4)$$

2.2. Experimental setup

Figure 2.3 shows the 70 m long KATRIN experiment and its main components. In the following the different sections will be explained separately.

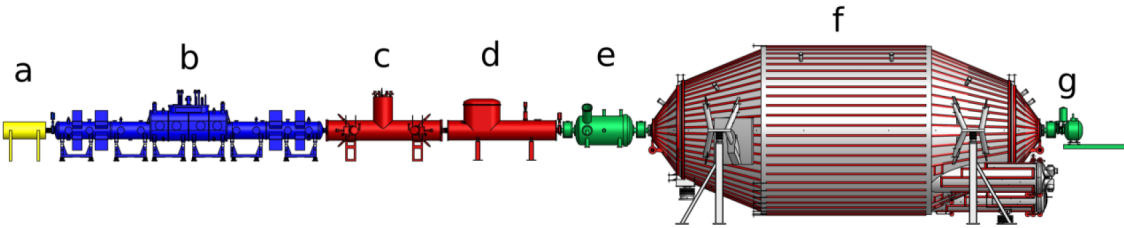


Figure 2.3.: The KATRIN experiment a) Rear section, b) windowless gaseous tritium source, c) and d) are the differential and cryogenic pumping sections, e) pre-spectrometer, f) main spectrometer and g) detector. The whole setup is about 70 m long.

2.2.1. The windowless gaseous Tritium source (WGTS) and the rear section

The WGTS source is formed by a 10 m long tube with an inner diameter of 90 mm, operating temperature of 30 K and an injection pressure of about 10^{-3} mbar. In the middle of the tube tritium molecules (T_2) are injected at a rate of $5 \cdot 10^{19} \frac{1}{s}$. These molecules diffuse to both ends of the tube. The rear section is monitoring the source continuously. At both ends of the source the tritium molecules are pumped out of the tube by turbomolecular pumps into the "inner loop" [Stu10] where they are recycled and injected again. The tritium decay rate is $10^{11} \frac{1}{s}$. Even at this high activity level there are only a few electrons with an energy very close to the endpoint of the β -spectrum (see figure 1.7).

In order to constrain the systematic error to the same magnitude as the statistic one, the column density of the WGTS has to be stable within 0.1%. Therefore the beamtube temperature has to be stable at $\Delta T < 30$ mK and the injection pressure has to be stable within 0.1%.

In the source tube a magnetic field (3.6 T - 5.6 T) guides the electrons on cyclotron trajectories to the spectrometers (and to the rear section). The magnetic field at the source is smaller than at the remaining setup, so a part of the electrons with large starting angles is reflected back before traversing the spectrometers (most are reflected at the DPS at $B = 5.6$ T). The maximal starting angle is about 51° and defined by the so-called pinch magnet operating at $B_{max} = 6$ T.

2.2.2. Pumping section

To keep the overall background rate at the detector in the few Hz range tritium must not get into the main spectrometer. Therefore the tritium flow has to be reduced 14 orders of magnitude which is done by combining two methods: in the first half of the pumping section the tritium flow is reduced by turbomolecular pumps (differential pumping section), in the second part the tritium molecules are adsorbed on an argon frost layer at 3-5 K (cryogenic pumping section). In each part the number density is reduced by about seven orders of magnitude. An important aspect in this regard is the existence of chicanes to avoid a beaming effect for tritium molecules which otherwise would penetrate into the spectrometer.

Of course the electrons are guided magnetically at 5.6 T throughout the whole pumping section.

2.2.3. Pre- and main spectrometer

The spectrometer section consists of two electrostatic integrating highpass filters operating as MAC-E-Filters (see chapter 2.1).

The pre-spectrometer is 3.38 m long and has an inner diameter of 1.68 m. It can filter out electrons with energies smaller than a fixed retarding voltage, e.g. 18.3 keV, to eliminate all electrons without information about the neutrino mass. These electrons could cause background in the main spectrometer by ionising residual gas. The pre-spectrometer is also used as prototype for test measurements before the commissioning of the main spectrometer. On the other hand, this tandem spectrometer-setup bears the risk of creating a Penning trap in which electrons can be stored, which may lead to uncontrollable discharges. The ideal operation parameters still need to be established. The pre-spectrometer also serves as tritium pumping section to further reduce potential tritium migration of the main spectrometer.

The main spectrometer has a diameter of 10 m and is 23 m long. Its task is to analyze the β -electrons close to the end of the tritium spectrum. Its resolution will be set to 0.93 eV (see equation 2.3) and the diameter of the source requires a large diameter of the flux tube of about 9 m in the analyzing plane. During measurements the tank is at -18.4 kV; this high voltage has to be stable at the ppm-level and is constantly monitored by two high voltage dividers and a third spectrometer - the monitor spectrometer (see chapter 2.2.5). Inside the tank there are two layers of wire electrodes which are operated on a slightly more negative potential (100 V respectively 200 V) than the tank, so that the resulting potential is 18.6 kV. With this wire electrode almost all electrons that resign from the tank walls² are prevented from penetrating into the flux tube where they would cause background. Two air coil systems are surrounding the spectrometer: The **E**arth **M**agnetic **F**ield **C**ompensation **S**ystem (EMCS) compensates the magnetic field of the earth and the **L**ow **F**ield **C**ompensation **S**ystem (LFCS) is used to fine tune the low field section of the magnetic field and detains the magnetic field lines from spreading out of the spectrometer.

2.2.4. Focal plane detector

The detector finally determines the number of the electrons that had enough energy to pass the retarding voltage. It consists of a Silicon PIN-diode with 90 mm

²induced by cosmic ray muons for example

diameter covering the whole flux tube. It has 148 segments to compensate the inhomogeneities in the electrostatic retarding potential and in the magnetic guiding field allowing to generate different transmission functions.

The background signal rate has to be smaller than a few mHz, requiring a passive and an active shielding of the detector. Additionally the electrons can be accelerated with up to 30 keV to transfer the signal band to energies in a region with less intrinsic background. The energy resolution of the detector is about 1 keV FWHM³.

2.2.5. High voltage monitoring

The high voltage of 18.6 kV at the analysing plane has to be stable at the ppm level (± 60 meV). By looking at figure 2.4 it can be seen that this is a decisive point for KATRIN. This accuracy has to be met over the whole measurement time of KATRIN, which is five to six years (the net measurement time of three years is prolonged by measurement breaks required for calibration and maintenance).

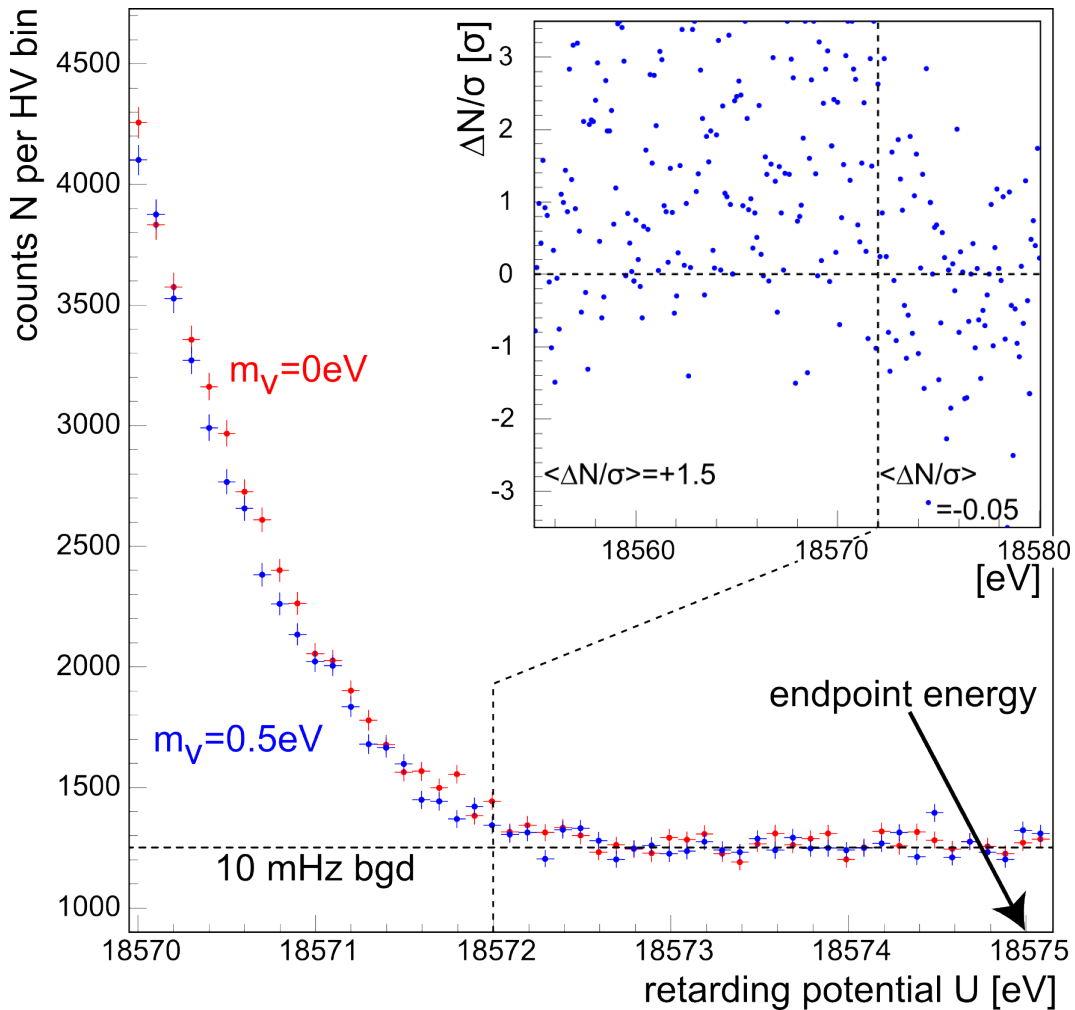


Figure 2.4.: Simulation of one year KATRIN measurements Typical integral β spectra including a constant background of 10 mHz for two values of the neutrino mass: $m_\nu = 0$ eV (red; upper dots) and $m_\nu = 0.5$ eV (blue; lower dots). The diagram in the right upper edge shows that only the part up to 18572 eV can be used for KATRIN and even there it is quite difficult to distinguish the values of the two neutrino masses. Thus it is necessary to know the retarding voltage very precise. [KAT05]

³Full Width at Half Maximum

The **monitor spectrometer** as a central element to monitor high voltage fluctuations works like the other spectrometers as a MAC-E-Filter. It continuously measures a monoenergetic calibration line of a driftless nuclear standard. To monitor the high voltage of the main spectrometer it is connected to the same power supply.

The monitor spectrometer has a separate beam line and is located in its own building to minimize the influence of stray fields. In the following chapter the monitor spectrometer will be described in more detail.

The other method to monitor the actual high voltage value makes use of two precise **high voltage dividers** that were build especially for KATRIN [Thü07]. They transform the high voltage into a low voltage range around 10 V which can be measured accurately by precision voltmeters.

3. The monitor spectrometer

To setup the monitor spectrometer beamline the spectrometer from the former Mainz neutrino mass experiment was transferred to KIT. The features of the former setup are described in more detail in [KBB⁺]. After the completion of the tritium measurements in Mainz were finished the spectrometer was modified to fit better into the KATRIN setup (see [Fla04] and [Mül02]).

In the following the components of the monitor spectrometer currently used for preliminary measurements are described in detail.

3.1. The spectrometer



Figure 3.1.: Monitor spectrometer, consisting of the thermally insulated tank, the two superconducting solenoids and the air coils.

The tank of the spectrometer is 1 m in diameter and 3 m in length. Contrary to the pre- and main spectrometer, where the tank itself is put on high voltage, the monitor spectrometer has a cylinder electrode inside on which the high voltage is applied to. The cylinder electrode is isolated against the tank which is grounded. Inside the cylinder electrode there is a wire electrode where a potential difference of 5 kV against the cylinder electrode can be applied.



Figure 3.2.: Cylinder- and wire electrode are seen in a configuration where the spectrometer was disassembled for the transport. In the background the stainless steel tank and three air coils are visible.

The main purpose of the monitor spectrometer is to measure the K_{32} -line of ^{83m}Kr , which has a width of 2.83 eV. For these reasons, the original resolution of 4.8 eV for 18.6 keV electrons had to be improved. The new resolution of 0.92 eV for 17.824 keV electrons is almost identical to the one of the main spectrometer; it corresponds to the Mainz-06 configuration described in [Thü07](see figure 3.3). At this high resolution the luminosity is smaller but this fact is only of minor importance as the monitor spectrometer will be coupled to a high count rate source. Also, the size of the sources is smaller than the one of the tritium sources, so the transported flux tube can be smaller as well.

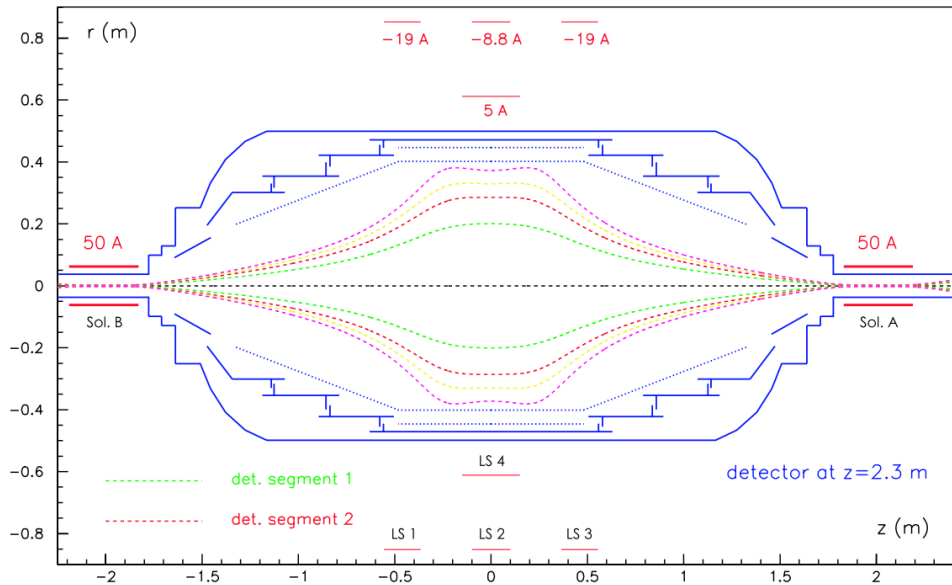


Figure 3.3.: Magnetic field configuration for the Mainz-06 setup with the tank, the cylinder electrode and the dotted wire electrode. The dashed lines illustrate the magnetic field lines. The electric current of the air coils is given. The maximal magnetic field at $z = 2.01\text{ m}$ is $B_{max} = 6.014\text{ T}$ and the minimal field in the analyzing plane is $B_{AP} = 3.09 \cdot 10^{-4}\text{ T}$ implying a magnetic field ratio of 19463:1 which corresponds to a resolution of 0.92 eV for 17.825 keV electrons. [Thü07]

3.2. Vacuum system

The ultra high vacuum (UHV) system has to provide a stable operation in the pressure regime of about 10^{-10} mbar. It is described in chapter 3.2.1. The first measurements and the present status of the system will be presented in chapter 3.2.2.

3.2.1. Principle

The main principle of the vacuum system can be seen in figure 3.4: A scroll pump (SC5D) creates a vacuum smaller than 1 mbar. One TurboMolecular Pump (Leybold MAG W 300) is responsible for an intermediate vacuum $< 10^{-5}$ mbar in an "intermediate vacuum tube" which is connected to the other three TMPs (with pneumatic valves in between). These are connected to the detector chamber (Leybold Turbovac 340 M), to the source chamber (Leybold MAG W 1500) and to the tank (Leybold MAG 2000). The TMPs are maintenance free, only the scroll pump has to be serviced after about 8000 hours of operational time. Thereby a vacuum buffer with a volume of 100 ℓ was installed to reduce the operation time of the scroll pump significantly. The TMP MAG W 300 has a pumping speed of 300 ℓ/s - therefore the pressure increases about 1 mbar per hour. As the MAG W 300 is able to pump against 8 mbar, it will be enough to operate the scroll pump three times a day for about one hour.

The possibility to perform a well-defined bake-out process prior to pump down is of course an important prerequisite to reach the required pressure (see chapter 3.3 for details).

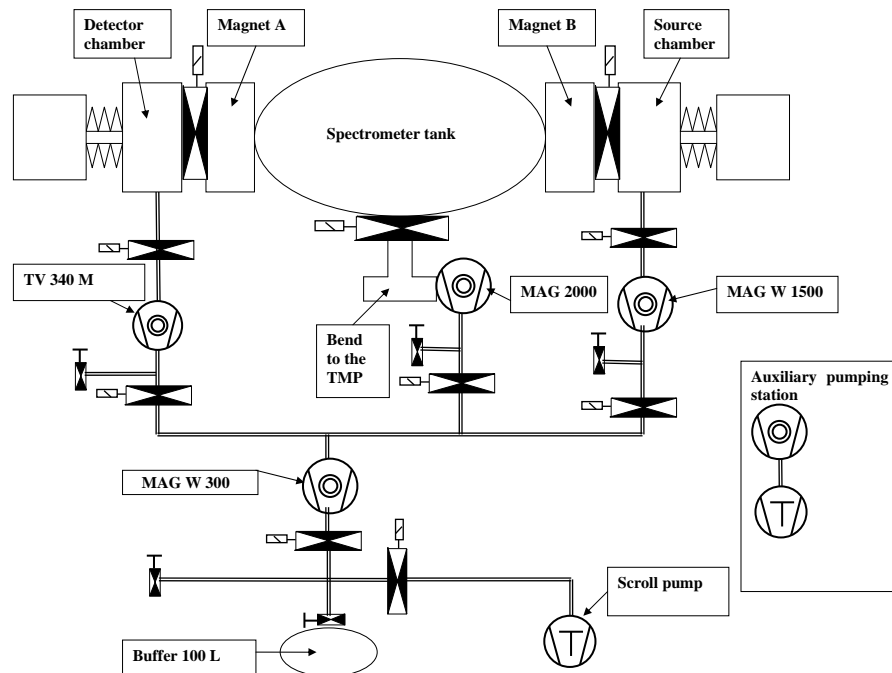


Figure 3.4.: Vacuum pumps at the monitor spectrometer

The monitoring of the vacuum system is shown in figure 3.5. There are two Pirani (robust thermal conductivity) gauges before the first TMP. To control the high vacuum there are two Leybold Ionivac ITR 90 and two Pfeiffer HPT100 gauges which use a combination of a hot cathode Bayard-Alpert gauge for low pressure and a pirani gauge for high pressure to sense the pressure from $1 \cdot 10^{-9}$ up to 1000 mbar. The three Leybold IE 514 gauges are for ultra high vacuum; they sense the pressure via hot cathode extraction type gauges down to $2 \cdot 10^{-12}$ mbar.

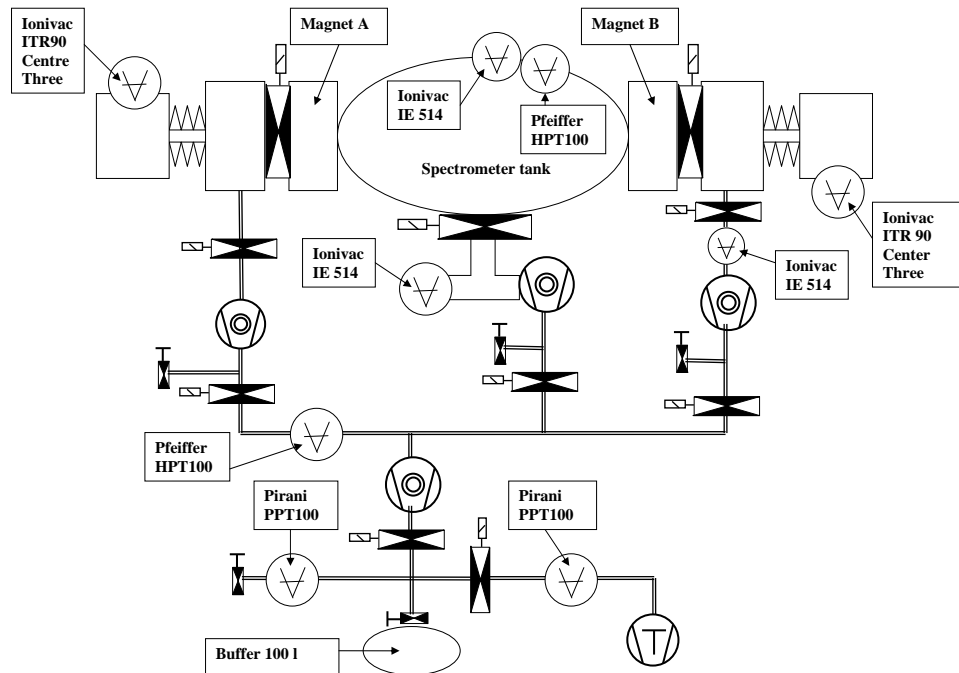


Figure 3.5.: Pressure sensors of the vacuum system

3.2.2. Status and results

The hardware installation of the vacuum system is finished. As can be seen from figure 3.6, where the performance is displayed over a time period of several weeks, it is fully functional.

Up to now the whole vacuum system was controlled manually, as the software controlling system PCS7 was being installed only during the last weeks of this thesis.

The results of the longest vacuum test so far are shown in figure 3.6. The end pressures reached of $2.1 \cdot 10^{-10}$ mbar in the spectrometer tank and of $1.2 \cdot 10^{-9}$ mbar in the source chamber are similar to the values reached in Mainz during their measurements. In the preliminary detector chamber (without the detector itself) a vacuum of 10^{-8} mbar was reached after only a few days of pumping, so also this part should not be problem.

Summing up one can state that the vacuum system is finished and can be used for measurements.

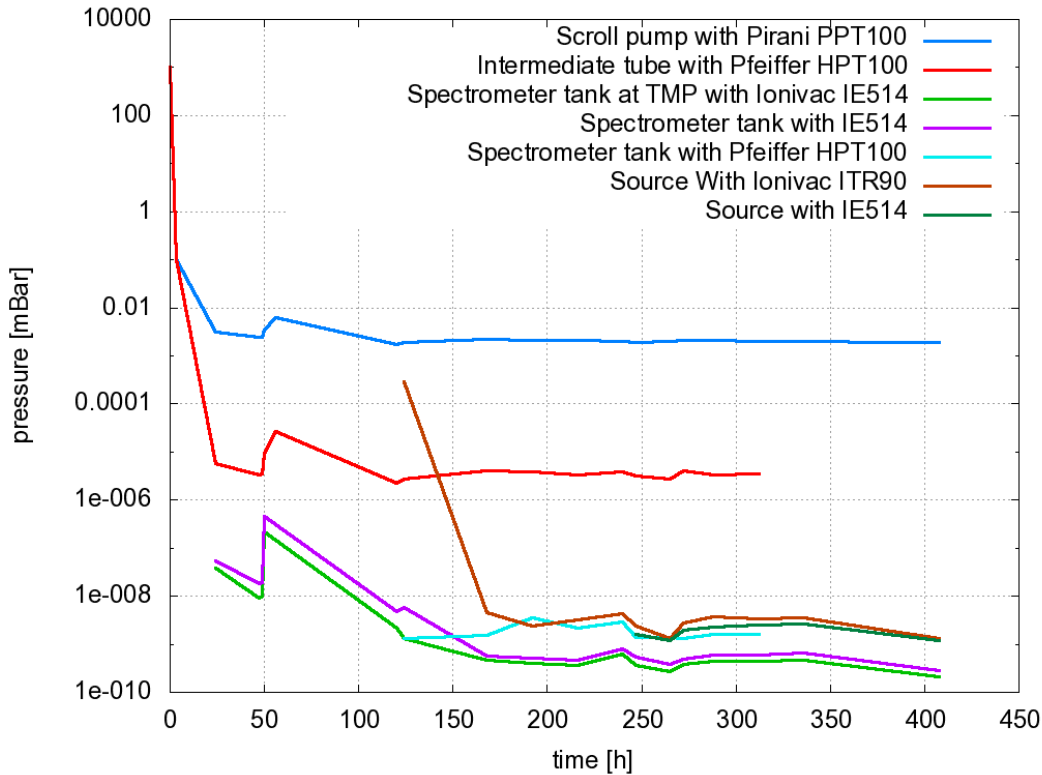


Figure 3.6.: Pressure development over several weeks The pressure of the fore-vacuum is about several 10^{-3} mbar, in the intermediate tube about several 10^{-6} mbar. The gauges in the spectrometer tank showed a pressure of $2.1 \cdot 10^{-10}$ mbar after 17 days of pumping. The final pressure in the source chamber was $1.2 \cdot 10^{-9}$ mbar. The detector chamber was not installed at this measurement. The increase of the pressure after 50 hours of pumping was due to some tests of the heating system.

3.3. Heating system

The heating system has the task to allow a bake out of the spectrometer at 200°C . Therefore heating wires are placed on the vessel hull, the detector and the source chamber, which can be controlled separately. The whole system is monitored by many resistance thermometers (PT100 sensors).

Up to now only one test of the heating system at the spectrometer tank has been performed, the systems at the source and the detector chamber are not operational at the time of writing.

The test was done with a preliminary Labview program that will later be substituted by the final PCS7 system as soon as system programming is finished. The test run which was performed in the framework of this thesis was successful - the tank was heated up to 200°C which is sufficient for the monitor spectrometer.

The improved heating system was installed to systematically investigate potential changes in the spectrum due to pressure variations in the tank. The Mainz measurement indicated that even a temporal increase in pressure can result in a shift of the line position. This is attributed to gas adsorbed onto the surface of the inner tank.

3.4. High voltage

The high voltage supply of up to 35 kV is already cable-connected to the cylinder electrode. It is supplied by the power supply unit FUG3. This system was tested without magnetic field and works stable at 35 kV.

In the near future one of the high voltage dividers will be installed at the monitor spectrometer to monitor the voltage precisely.

3.5. Magnetic System

The two superconducting magnets are solenoids from Oxford-Instruments Limited with a maximum magnetic flux density of 8.6 T at 71.48 A. They are operated at 4.2 K requiring cooling with liquid helium. Their distance to the analysing plane is 2.01 m. In normal mode of the monitor spectrometer they are operated at 50 A which corresponds to a magnetic flux density of 6.014 T.

After transport and installation in the monitor building they were tested at 7.2 T (60 T). For the test value of $B = 7.2$ T a map with lines of the same magnetic field is shown in figure 3.7.

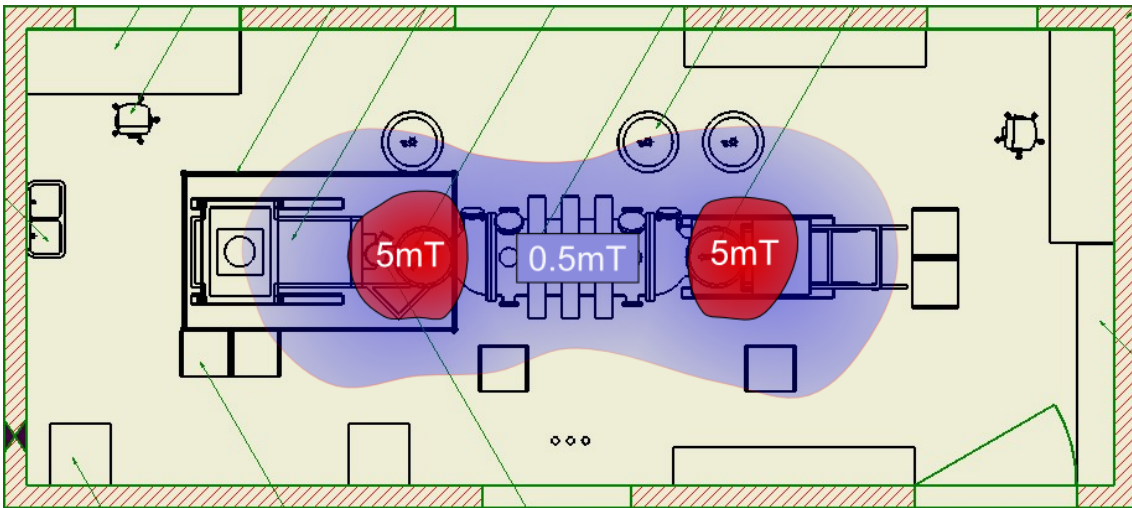


Figure 3.7.: Magnetic field line contour for a maximum magnetic flux density of 7.2 T at the center of the solenoids.. Inside the red area the field is higher than 5 mT, inside the blue area it exceeds 0.5 mT. Normal equipment can be exposed to fields up to 5 mT whereas 0.5 mT is the safety margin for persons with specific medical implants like pace makers.

3.6. Air coil system

The monitor spectrometer is surrounded by two air coil systems: the EMCS (**E**arth **M**agnetic **F**ield **C**ompensation **S**ystem) and the LFCS (**L**ow **F**ield **C**ompensation **S**ystem). These can be seen in figure 3.1. The LFCS consists of four air coils around the vessel - thus forcing the magnetic field lines to being confined to the inside of the tank, so that the electrons do not hit the walls (see figure 3.3). The EMCS consists of the horizontal white tubes. It compensates the magnetic "background" which mainly consists of the magnetic field of the earth. Chapter 4 describes the test measurements with these systems.

3.7. The Source

The source has to provide electrons at energies close to the endpoint energy of tritium with high counting rates. In this chapter the setup of the source part will be described, the different possible sources will be presented and their suitability is discussed.

3.7.1. The source part of the spectrometer

The actual setup of the source area can be seen in figure 3.8. The base frame of this unit was rebuilt at KIT because the old one from Mainz could not be used for further measurements.

During later routine measurements the pressure inside the chamber should be about 10^{-9} mbar which can be achieved by a turbo molecular pump. Up to four sources can be placed on the sourceholder at the same time (see figure 3.9).

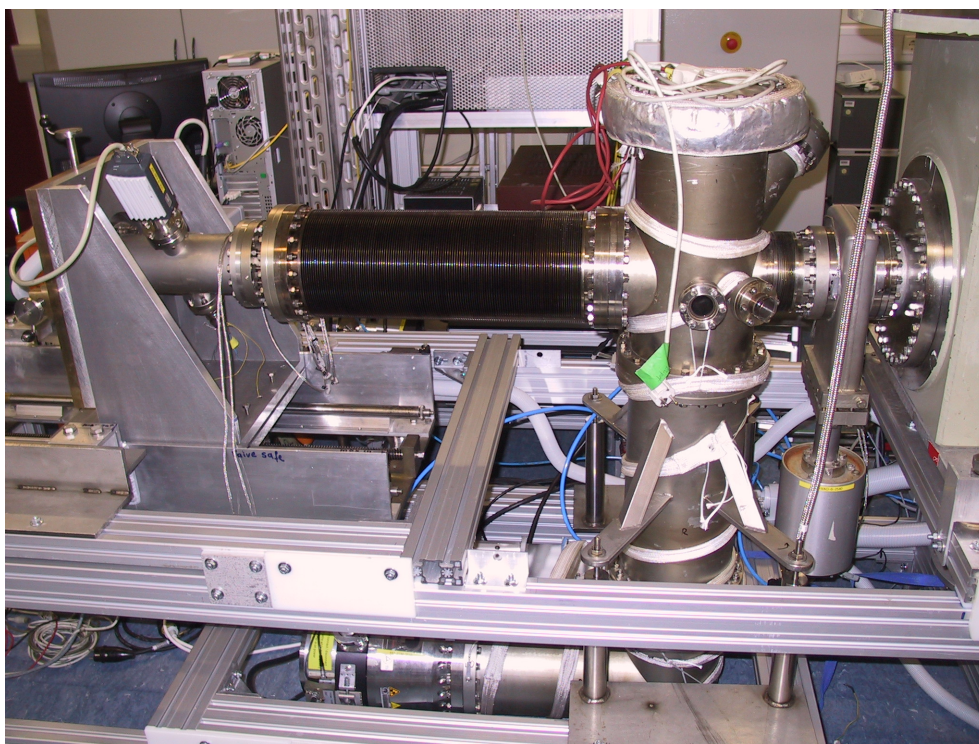


Figure 3.8.: The source part of the monitor spectrometer On the right side the magnet which is connected to the source chamber via a pneumatic valve can be seen. The source chamber is connected to the cross table with a diaphragm bellows. Below this the source-TMP is installed.

The source holder is connected to a movable tube which can be displaced in axial and radial direction. The radial motion is obtained by a new cross table made in Řež/Prague, which allows a motion of 20 mm in every direction. The old one allowed a movement of only 10 mm and is now used for the detector vacuum chamber.

The axial movement the sources allows to position them in different magnetic fields (see figure 3.10). It also makes it possible to easily change the sources. As there are four sources on the sourceholder, the radial movement is needed to position one of them into the center.



Figure 3.9.: Sourceholder The left side shows the sourceholder. The sources sit on banana plugs, which can be plugged into the respective banana socket. Behind the ceramic plate the centering cross made out of spring bronze can be seen. The cross is electrically isolated so that it can be detected when it touches the wall. Visible are also the cables which allow to set the potential on each source individually. On the right side the tube on which the sourceholder is placed can be seen.

Additionally there is the possibility to apply a specific potential to a single source to shift its energy spectrum. The functionality of the potential option has partially been tested. The feed-through and the ceramics can handle up to 1 kV but the cables are not tested yet.

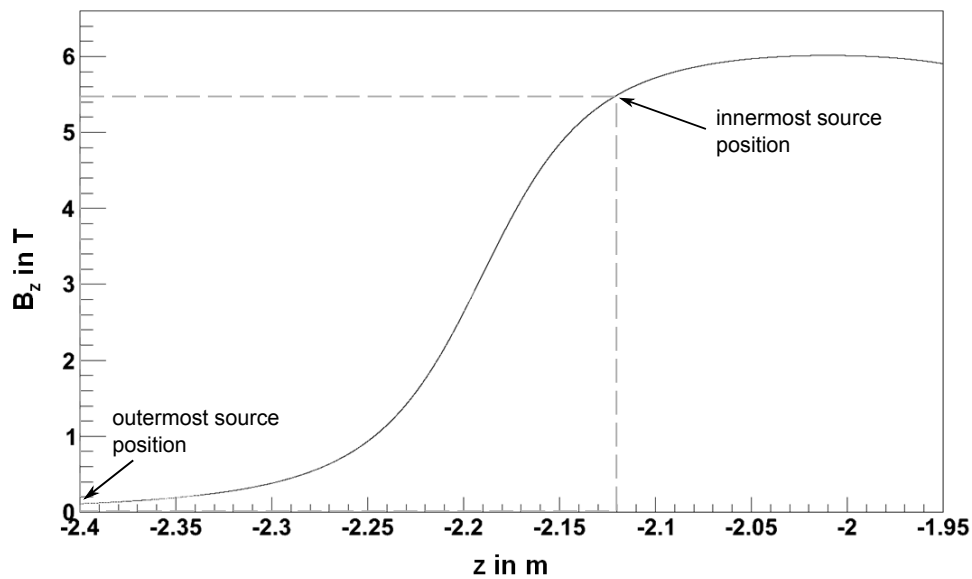


Figure 3.10.: Magnetic field simulation at the source The source can be moved in axial direction, so that it can be positioned at different magnetic fields. This position will be from about $z = -2.40$ m to $z = -2.12$ m and hence the magnetic field can be chosen between 0.1 T to 5.4 T.

3.7.2. The different sources and their suitability

Three sources have been analyzed for their suitability for the calibration at the monitor spectrometer. The Am/Co source [Kas08] generates electrons with 18.6 keV and has a FWHM of 1.3 eV. The other two ones (Condensed Krypton Source (CKrS) [Ost08] and Solid Krypton Source (SKrS) [Zbo10]) both use krypton with an electron

energy of 17.8 keV and a FWHM of 2.8 eV. Whereas the Am/Co source is very close to the tritium endpoint energy, the difference for krypton is 0.8 keV - implying that both sources are suitable for the use at KATRIN.

3.7.3. The $^{241}\text{Am}/\text{Co}$ Source

The $^{241}\text{Am}/\text{Co}$ Source uses photoelectrons that are induced by γ -radiation. The γ -radiation from ^{241}Am has an energy of $E_\gamma = 26344.6(2)$ eV. It strikes a thin cobalt foil, where electrons are released from the K-shell. Their energy is [Thü07]:

$$E_{kin} = E_\gamma - E_{b,F} - E_{e,rec} - \phi_{filt} \quad (3.1)$$

where E_{kin} is the energy of the electrons, E_γ denotes the γ -ray energy and $E_{b,F}$ the energy relative to the Fermi level. The recoil energy transferred to the nucleus is $E_{e,rec}$ and the work function of the filter electrode of the spectrometer is ϕ_{filt} . This work function has to be considered because it modifies the retarding potential of the spectrometer directly (as seen in figure 3.11).

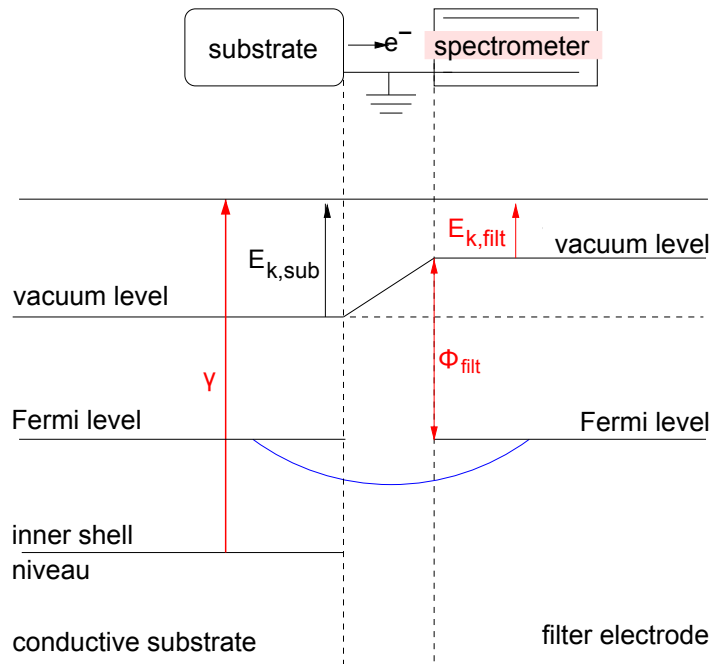


Figure 3.11.: Influence of the work function At two contacted conducting materials the Fermi levels adjust themselves. The vacuum levels do not because of the work function ϕ_{filt} of the filter electrodes. The measured energy is $E_{k,filt}$ and not $E_{k,sub}$. [Ost08]

The ^{241}Am isotope has a half life of 432 years allowing the possibility of long-term monitoring with this calibration source. The small width and the minor difference to the endpoint energy of tritium make this source very promising. But there are some problems: the background-to-signal-ratio was only 1 to 4 (at measurements in Mainz) which caused a long measurement time. Moreover some energy loss in the source was observed (see figure 3.12).

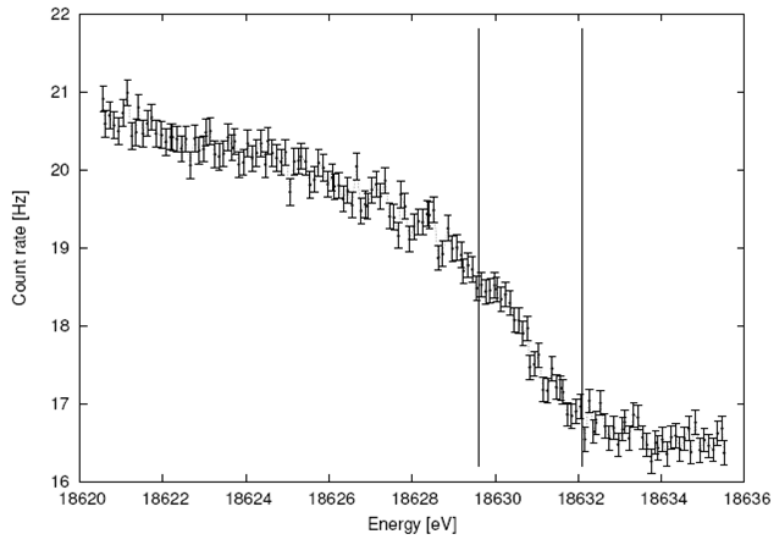


Figure 3.12.: Integrated spectrum of the Am/Co source In this diagram the problems with this source can easily be seen: There is a very low count rate of about 18 Hz. At a background of more than 16 Hz the important part goes up to only 19 Hz so only a difference of 3 Hz is used for analysis. The energy loss in the source is visible at lower energies where the count rate is still rising. [Kas08]

3.7.4. The $^{83}\text{Rb}/^{83\text{m}}\text{Kr}$ -Sources

The $^{83}\text{Rb}/^{83\text{m}}\text{Kr}$ -sources makes use of the decay of $^{83\text{m}}\text{Kr}$, which is produced by electron capture of ^{83}Rb (see figure 3.13). The position and width for the different transitions are given in table 3.1.

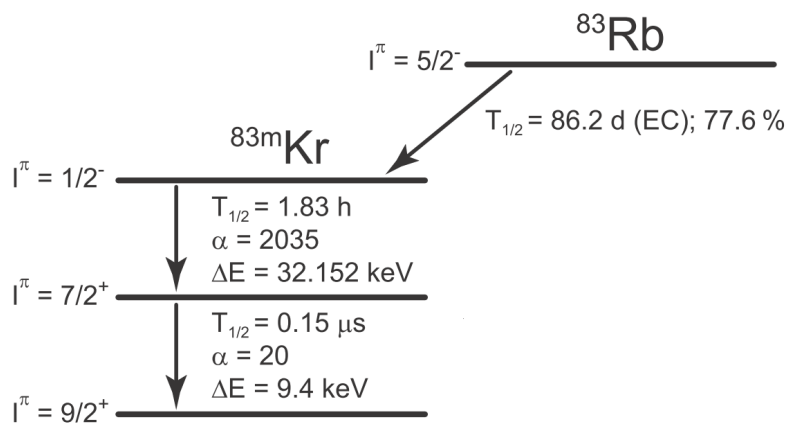


Figure 3.13.: Decay scheme of rubidium ^{83}Rb , which decays by electron capture into $^{83\text{m}}\text{Kr}$. This isotope reaches the ground state by two highly converted γ -transitions. The conversion coefficient α is the quotient of the emitted conversion electrons and the non converted γ quanta. [Ost08]

Table 3.1.: Conversion electron energy of the 32 keV transition of ^{83m}Kr as determined in [Ost08]. σ_l and σ_g are the fitted values for the width; l stands for Lorentzian and g for gaussian distribution. If both values are given the spectrum was fitted with a Voigt function.

level	name	amplitude in 1/s	position in eV	σ_l in eV	σ_g in eV
$1s_{1/2}$	K	440 ± 15	17826.309 ± 0.001	2.70 ± 0.06	
$2p_{1/2}$	L_{II}	353 ± 3	30421.856 ± 0.020	1.165 ± 0.069	
$2p_{3/2}$	L_{III}	587 ± 2	30474.575 ± 0.006	1.108 ± 0.013	0.388 ± 0.0001
$3p_{1/2}$	M_{II}	58.6 ± 0.5	31931.274 ± 0.006	1.230 ± 0.061	0.403 ± 0.027
$3p_{3/2}$	M_{III}	105 ± 0.3	31938.960 ± 0.006	1.322 ± 0.018	0.403 ± 0.027
$4s_{1/2}$	N_I	0.8 ± 0.4	32124.625 ± 0.963	$0.4 \pm \text{fixed}$	
4p	N_{II}/N_{III}	224 ± 1	32139.377 ± 0.010		0.608 ± 0.013

3.7.4.1. Condensed $^{83}\text{Rb}/^{83m}\text{Kr}$ -Source (CKrS)

For the condensed krypton source the electron emitter ^{83m}Kr is condensed onto a graphite plate (HOPG¹). Therefore ^{83m}Kr -gas produced by ^{83}Rb decay was led to the graphite plate, which was cooled down to 20 K so that krypton gas was frozen onto the graphite surface.

For this gaseous source the kinetic energy of the K-32 conversion electrons is given by [KAT05]:

$$E_{Kin} = E_\gamma + E_{\gamma,rec} - E_b^{vac} - E_{e,rec} - (\phi_{spectr} - \phi_{source}) - C \quad (3.2)$$

Here, E_γ is the γ -ray energy, E_b^{vac} is the binding energy of K-shell electrons related to the vacuum level, $E_{\gamma,rec}$ is the energy of the recoil atom after γ -ray emission and $E_{e,rec}$ is energy of the recoil atom after emission of the conversion electron. The parameters ϕ_{spectr} and ϕ_{source} are the work functions of the retarding electrode and of the source, respectively the term C accounts for possible space and surface charges within the gaseous source.

To obtain a sufficiently clean and homogeneous ^{83m}Kr -layer the substrate had to be cleaned and controlled. For the cleaning three different methods were tested (preplating, heating and ablation, see figure 3.14). The controlling was done by laser ellipsometry.

An initial problem resulted from the residual gas which modified the work function and the binding energy. As the binding energy and the work function change the electron energy, the residual gas caused instabilities.

Once all these problems were under control this source was quite stable (see figure 3.14) and reproducible. The major experimental disadvantages are the facts that it cannot be operated continuously and that the setup is rather complex.

¹Highly Oriented Pyrolytic Graphite

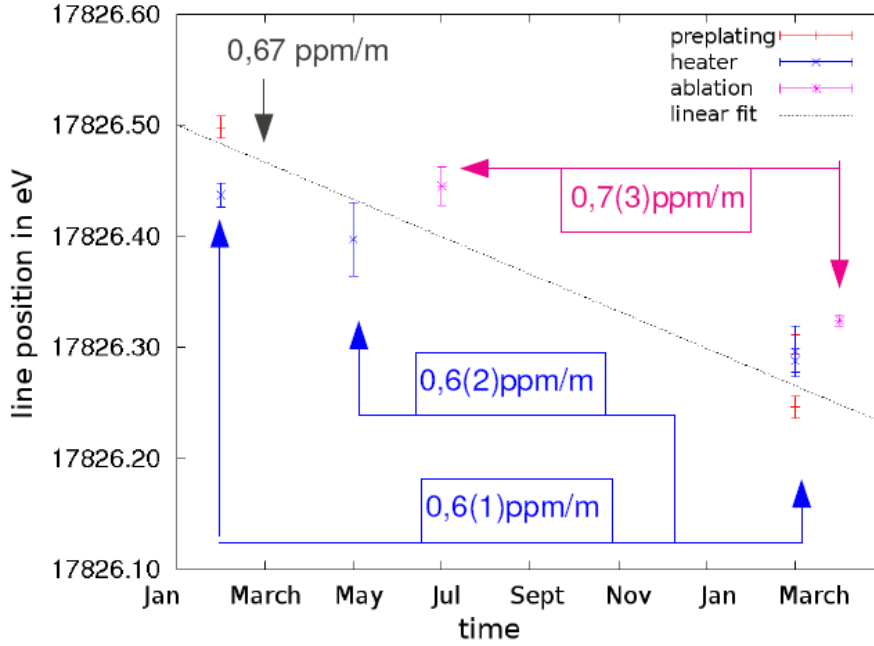


Figure 3.14.: Results from the CKrS in Mainz Here the stability of the condensed krypton source is displayed. During the measurement time of more than a year the drift is only about 0.6 ppm per month. This drift matches the drift from the high voltage divider, which was used in these measurements - so the krypton source should be stable on a much better level. Source: [Ost08]

3.7.4.2. Solid state $^{83}\text{Rb}/^{83\text{m}}\text{Kr}$ -Source (SKrS)

The solid state krypton source is produced by implantation of rubidium into a platinum or gold plate. It is again ^{83}Rb ($T_{1/2} = 86.2 d$) that is implanted because of the short half-life of $^{83\text{m}}\text{Kr}$ ($T_{1/2} = 1.83 h$).

The energy of the conversion electrons from the K-shell in the solid state source has no reference to ϕ_{source} :

$$\begin{aligned} E_{e,kin} &= E_{\gamma_{32}} + E_{\gamma_{32,rec}} - (E_{bin}^{Fermi,source} + \phi_{source}) - (\phi_{spectr} - \phi_{source}) - E_{e,rec} + C \\ &= E_{\gamma} + E_{\gamma_{32,rec}} - E_{bin}^{Fermi,source} - E_{e,rec} - \phi_{spectr} + C \end{aligned} \quad (3.3)$$

where $E_{\gamma_{32}}$ denotes the energy of the transition which has to be corrected by the recoil energy of the nucleus $E_{\gamma_{32,rec}}$. $E_{e,rec}$ is the energy of the recoil atom after emission of the conversion electron and $E_{bin}^{Fermi,source}$ is the Fermi energy of the source. ϕ_{spectr} and ϕ_{source} are the work functions of the spectrometer and the source and C is the potential energy shift in a solid state source.

The solid sources were made at the ISOLDE facility at CERN, Geneva. At ISOLDE a proton beam at 1.4 GeV hits a target. The resulting ions are mass separated. At the measurements the energy of the ^{83}Rb -ions was set to 30 kV. They were guided to the setup seen in figure 3.15, where they were implanted into a substrate. With the existing setup it was possible to make sources with energies between 15 and 30 kV implantation energy. This rather complicated setup is used to achieve an energy

high enough so that the krypton is retained - but at low depth so that a significant fraction of the electrons comes out with no energy loss (see [Spa08]).

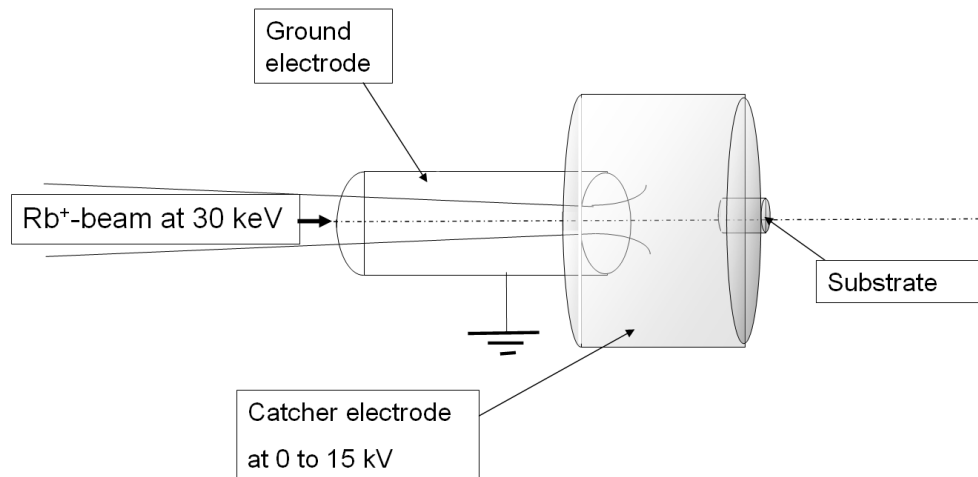


Figure 3.15.: Setup at ISOLDE facility The ^{83}Rb -beam with an energy of 30 keV impinging from the left was guided through a grounded electrode to be focused in the middle. The ^{83}Rb -ions were implanted in a substrate which was within a catcher electrode at voltages between 0 and 15 keV. [Zbo10]

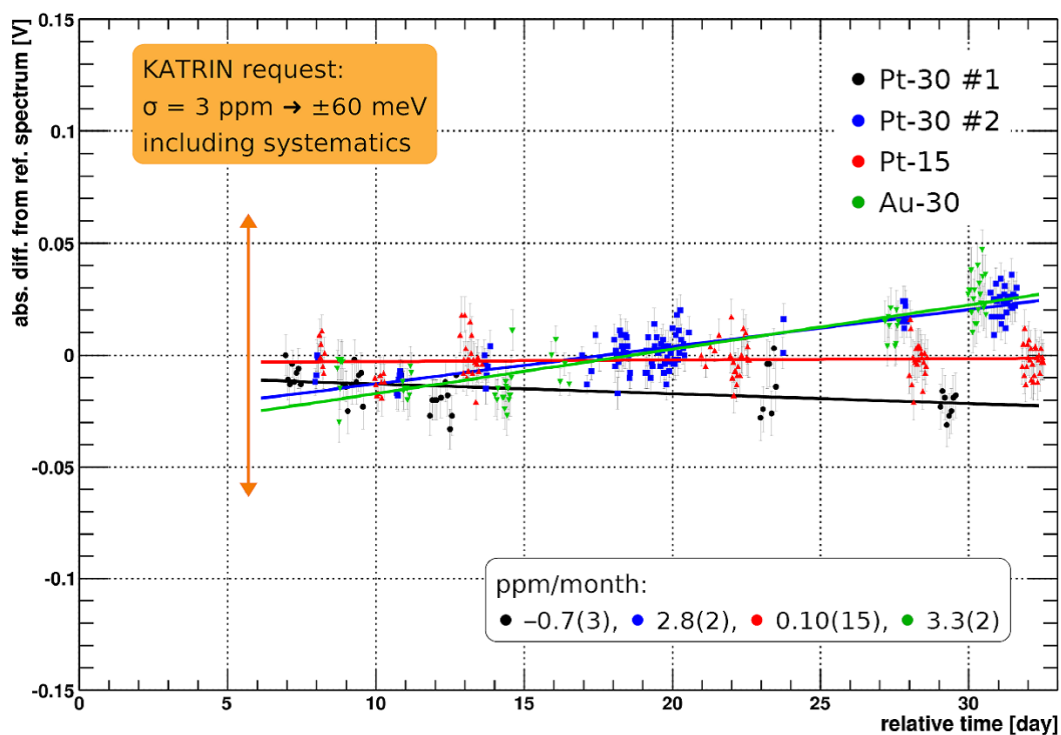


Figure 3.16.: Long-term stability of SKrS sources Here the shift of the line positions over a period of about 30 days can be seen. Four sources were analyzed: Pt-30 means that ^{83}Rb was implanted into platinum with 30 keV. The orange arrow shows the requirement of KATRIN. The best of these five sources is Pt-15 with a drift of only 0.1 ppm per month. But as the two Pt-30 sources differ strongly, further research is required. [Zbo10]

These sources are very easy to handle as their size is 14 mm in diameter. They are

reliable but there is a source to source difference of about half a volt. This fact can be circumnavigated because one source is adequate for one measurement period of KATRIN, which will be two months. Some of the analyzed sources display a long-term stability that meets the stringent requirements of KATRIN (see [Zbo10] and figure 3.16), but further research has to be done on this sources to improve their performance.

3.7.5. Conclusion

In summary it can be stated that the solid state krypton source is the most adequate choice for the monitor spectrometer. However, with only four sources being tested so far, the fact that some of them did not meet the requirements of KATRIN requires that more sources have to be made and analyzed. There were also some still unexplained structures in the spectra. The condensed krypton source has a very complicated set-up and will only be used to calibrate the pre- and main spectrometer.

3.8. Detector

The detector has to count the electrons that have passed the electrostatic potential in the spectrometer and consists of a silicon based semi-conductor PIN-diode.

To position the detector in the middle of the flux tube it is mounted on a cross table. For calibration, the whole detector platform can be moved in axial direction. The motion also allows to position the detector in different magnetic field strengths (similar to the source, see figure 3.17). The base frame and the vacuum chamber was rebuilt at KIT.

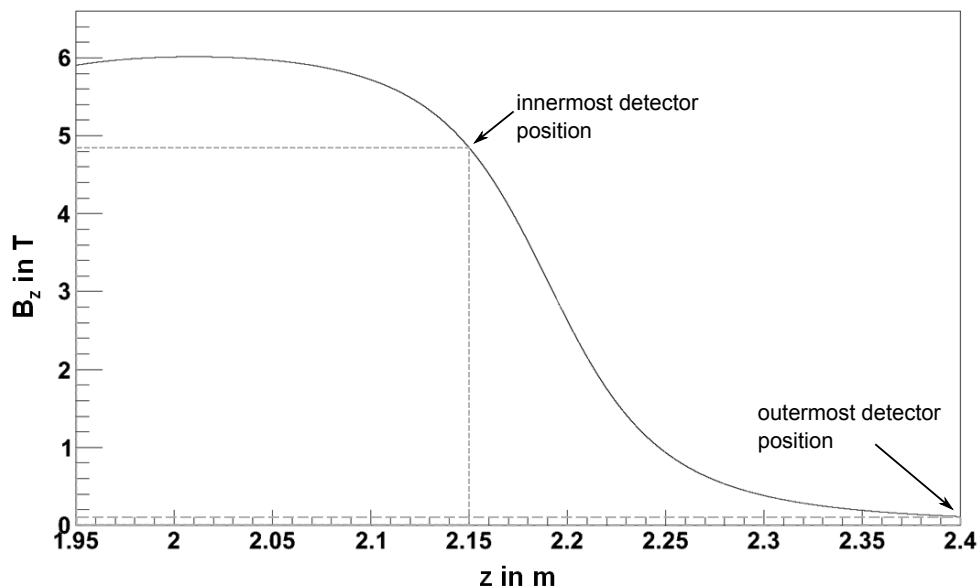


Figure 3.17.: Magnetic field simulation at the detector side The detector can be moved in axial direction so it can be positioned at different magnetic fields. This position will be from about $z = 2.15$ m to $z = 2.40$ m, hence the magnetic field can be chosen from about 4.8 T to 0.1 T.

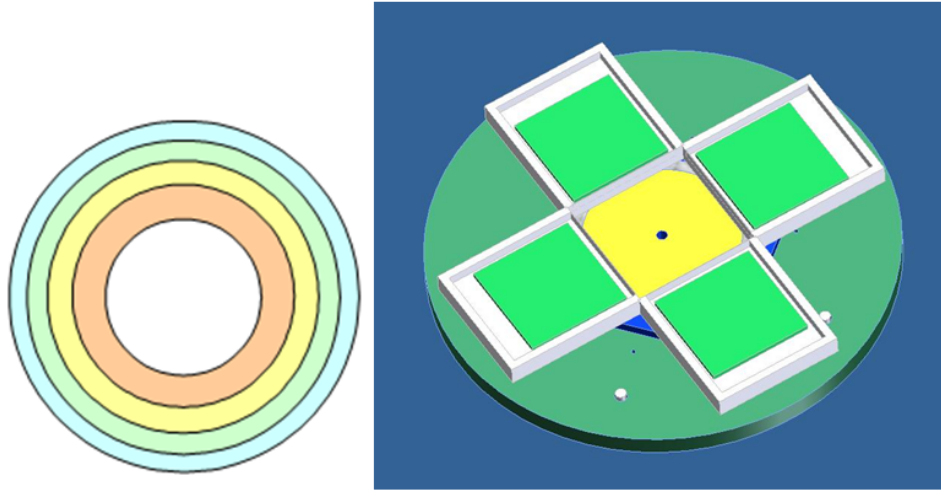


Figure 3.18.: Old and new detector On the left the old detector geometry that was used in Mainz can be seen. Every section has a size of 1 cm^2 , which corresponds to the size of the flux tube. The new detector on the right side differs in geometry and size. The central detector has a size of 1.5 cm^2 ; the four outer ones are $10 \times 10\text{ mm}$.

The old detector in Mainz had five circular elements with an area of 1 cm^2 each (see figure 3.18). The effective thickness was $500\text{ }\mu\text{m}$. This detector chip was connected to a copper cold finger which was cooled by liquid nitrogen (LN_2). Thus the energy resolution obtained was a few keV FWHM for 18.6 keV electrons.

The new detector consists of five separate silicon based based semi-conductors. This set-up is cheaper and the single elements can be replaced separately. As seen in figure 3.18 also their geometry has changed: now it is possible to determine the position of the flux tube. For the filter spectra only the central detector (a Canberra PD150-12-500AM) is used. It has a size of 1.5 cm^2 , an active thickness of $500\text{ }\mu\text{m}$, a FWHM of 7 keV and the dead layer is below 50 nm . For the four outer detectors Hamamatsu S3590-09 PIN diodes are used. Their active area is $10 \times 10\text{ mm}$ and their depletion layer is about $300\text{ }\mu\text{m}$ thick.

Due to some technical problems during set-up and assembly the detector was not ready for measurements within the time frame of this work. At the time of writing it is being installed at the monitor spectrometer paving the way for the first test measurements.

3.9. Slow control and data acquisition

The *slow control* units control the voltage and allow to pre-define the measurement time. It is based on the program package Labview from National Instruments. The input is provided by an excel file with data for the measurement procedure (voltage values and measurement time). It controls the high voltage supply which gives back the voltage value after it is reached. The values for the voltage and measurement time are saved in a text file. This can be upgraded so that the slow control data are written into the Zeus database.

The **PSC7** system controls the safety-relevant parts of the monitor spectrometer. These are the vacuum, heating and cryogenic systems. The PCS7 system could not be used in this work, as it was finished only during the last weeks of this thesis.

The **detector data** (impulses of the pre amplifiers) are digitised by a VME crate² which includes a trigger and a shaper. These data are passed to the ORCA³ system which converts the binary data via ORCARoot into ROOT histograms. These are then converted into crun files (also ROOT histograms).

3.10. Data analysis

The data analysis has to convert the data into an integrated spectrum. Therefore a preliminary analysis tool (called *ana_mospec*) was programmed within the scope of this work.

In the first step it plots the spectrum of each scan in one histogram and draws the integral limits for the peak rate and the pulser rate (see figure 3.19). These limits can be defined by the chanal number or by Gauss fits of the single spectra.

The next step is the dead time correction. The dead time correction factor is given by

$$\frac{f \cdot t}{n_p} \quad \text{with the error} \quad \sigma_{n,p} = \sqrt{f \cdot t - n_p} \quad (3.4)$$

where n_p is the pulser rate, f the pulser frequency and t the measurement time. Then the pulser rate is plotted over the total rate n_{total} and a linear function is fitted as seen in figure 3.20 (so $n_p = a \cdot n_{total} + b$ with the fitting parameters a and b). This fitting is done to minimize the errors. If this correction would be done for each point separately, the errors at the integrated spectra (figure 3.21) according to formula 3.6 would be much bigger.

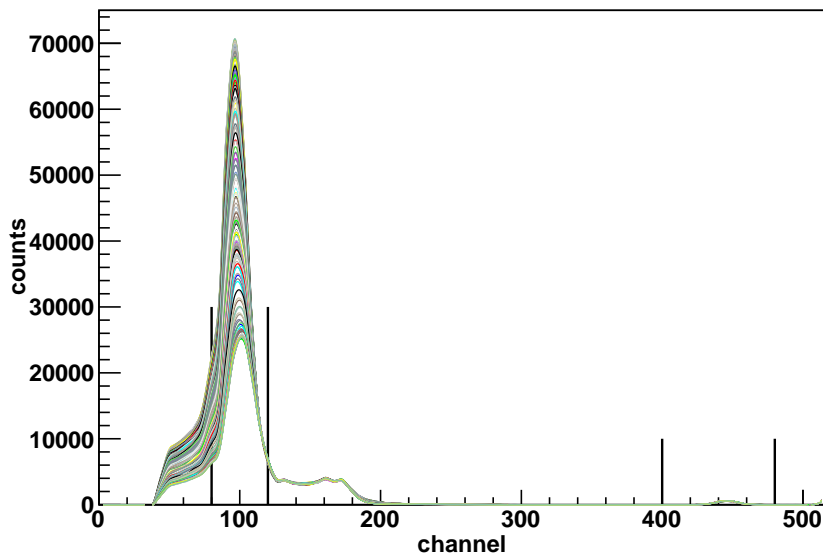


Figure 3.19.: Spectra of the K-32 conversion electrons Here the spectra of 189 measurements done in Mainz are plotted. The K-32 line is clearly visible at channel 100. The barely visible peak at channel 450 is generated by the pulser. The black lines mark the regions in which the counts are integrated for the integrated spectrum and the dead time correction.

²this crate will be replaced soon by an IPE V4 crate

³Object oriented Real-time Control and Acquisition

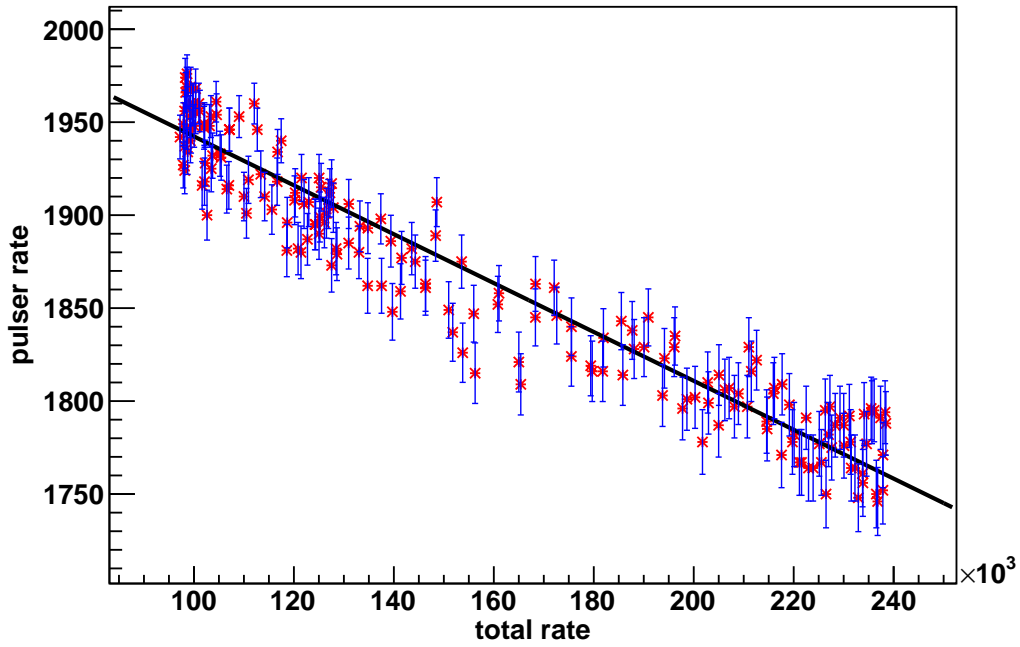


Figure 3.20.: For the **dead time correction** the pulser rate is plotted over the total rate. The errors are calculated with formula 3.4; the fitting is done with a linear function in ROOT.

Now the dead time corrected integrated spectrum can be plotted. The counts are integrated as shown in figure 3.19. The dead time correction is done by the following formula:

$$n_{dtc} = \frac{f \cdot t}{n_p} \cdot n \quad (3.5)$$

where n_{dtc} is the dead time corrected rate and n the uncorrected rate in the peak. The errors for the rates are calculated according to Poisson statistics:

$$\sigma_n = \frac{\sqrt{n \cdot t}}{t} \quad (3.6)$$

where n is denoting the count rate and t the measurement time.

For the error of the dead time correction the error of the total rate is used whereas the uncertainty of the fitting parameters a and b are neglected. The errors of the integrated spectrum are calculated with propagation of uncertainty:

$$\sigma_{n_{dtc}} = n_{dtc} \cdot \sqrt{\left(\frac{\sigma_{n,dtc}}{n_{dtc}}\right)^2 + \left(\frac{\sigma_{n,tot} \cdot a}{f \cdot t}\right)^2} \quad (3.7)$$

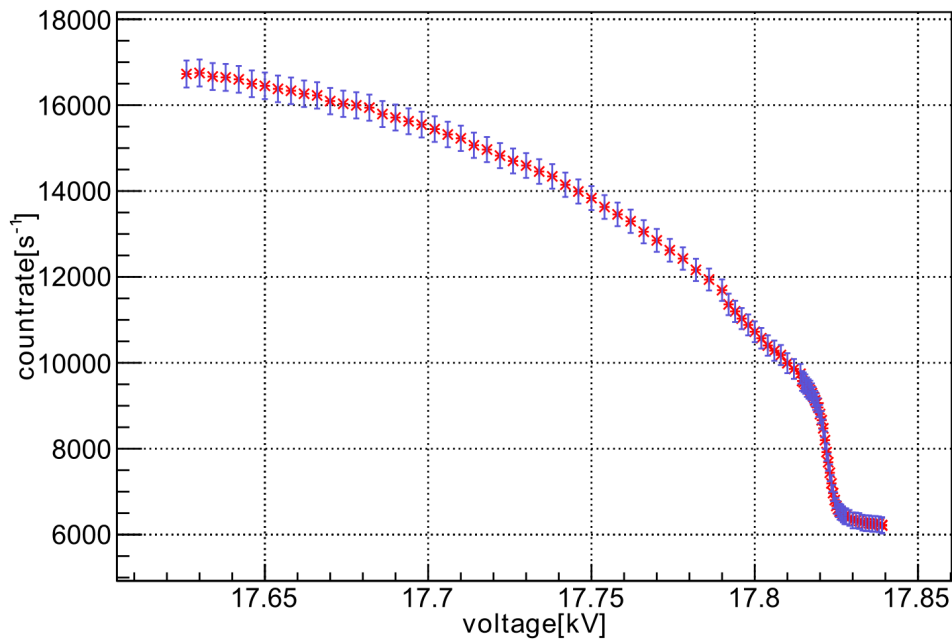


Figure 3.21.: Integrated spectrum For the integrated spectrum the integrated counts are drawn over the corresponding value of the voltage. In the majority of cases the counts and the voltage were measured twice (first the voltage was decreased, then increased until the starting point was reached again) - so for the integrated spectrum the average of the voltage and count rate values was used. The errors were calculated according to formula 3.7 and are multiplied by the factor ten to be visible in this plot.

The fitting of the integrated spectrum will be done by two different fitting routines programmed mainly by M. Zboril. The "traditional method" is used to fit the first spectrum. Therefore the spectrum is fitted with a Voigt function that is a convolution of the Gaussian with Lorentzian distribution. The spectra that are measured afterwards should have the same shape as the first one. For monitoring a much easier fit method can be used: The "reference method" uses the spectrum that was measured before and fits only the background, the amplitude and the shift in order to detect any changes in the line position.

4. The air coil system

The magnetic field in the monitor spectrometer is generated by two superconducting solenoids (see chapter 3.5). It decreases from a maximum value of 6 T inside the solenoids to $300 \mu\text{T}$ (about $1/20000$) in the analysing plane.

The air coil system is able to change the magnitude and the direction of the magnetic field. As described in chapter 3.6 it consists of the two components EMCS¹ and LFCS². The LFCS keeps the magnetic field lines inside the cylinder electrode (as seen in figure 3.3), and the EMCS compensates the magnetic field of the earth. The present magnetic field of the earth (about $50 \mu\text{T}$) contributes to about 16 % in the analyzing plane and has thus to be compensated. The EMCS system has already been tested successfully in an independent work in a separate test setup [Rei09].

In the following the measurements related to the external air coil system are presented and compared to corresponding simulations.

4.1. Magnetic field measurements

Each measurement point was done along the z-axis of the monitor spectrometer³. The analyzing plane is at $z = 0$ m, the x-axis runs horizontal and the y-axis vertical. The sensor used was a "Mag-03MS1000 Three Axis Fluxgate Field Sensor" from Bartington Instruments with a measurement range of up to $1000 \mu\text{T}$ in each direction and a precision of ± 100 nT (for more information see [Rei09]).

4.1.1. Background measurements

The measurement of the background field has yielded the expected values for the magnetic field of the earth. The spectrometer is positioned almost in north-east direction, so the y-component with about $40 \mu\text{T}$ is the biggest one, while the z-component is about $20 \mu\text{T}$ and the x-component is negligible (as seen in figure 4.1).

¹Earth Magnetic Field Compensation System

²Low Field Compensation System

³The z-axis proceeds along the longitudinal direction in the middle of the spectrometer ($x = y = 0$ m)

The specific decrease at $z = 1.5$ m is caused by magnetized rods at the spectrometer. This small magnetic anomaly should not have an effect on the later measurements as the magnetic field at this point is dominated by the magnetic field of the solenoids which will be about 40 mT at $z = 1.5$ m (this value is deduced from old magnetic field maps from Mainz). However, when the solenoids have been operated, the magnetic field caused by the rods will be higher and thus may have an effect on the magnetic field in the analysing plane. This should be further investigated by the time the spectrometer is taking data.

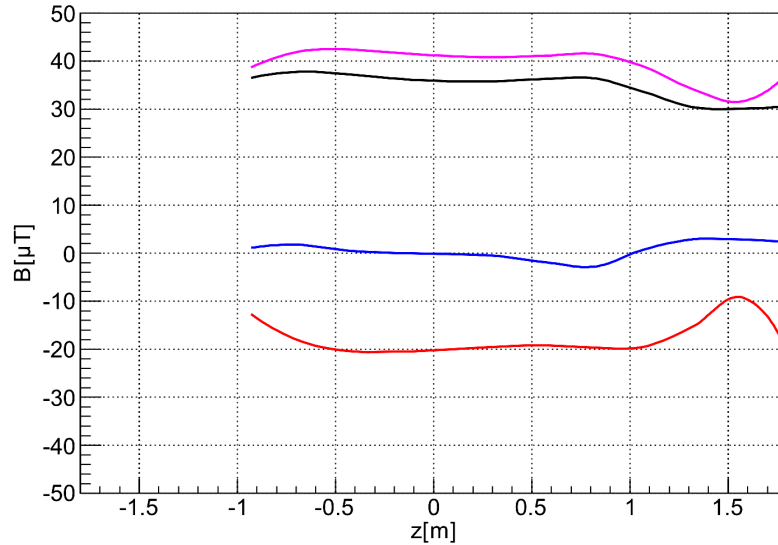


Figure 4.1.: Magnetic field background in the monitor spectrometer. From top to bottom: B_{total} is plotted in pink, B_y in black, B_x in blue, B_z in red.

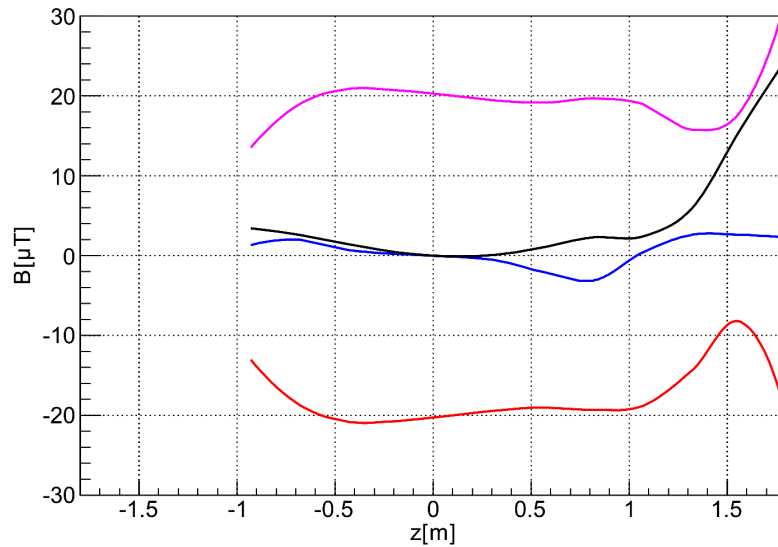


Figure 4.2.: Background compensation with the EMCS The EMCS system has compensated the y-component of the magnetic field. Therefore the x-component of the EMCS was operated at $I = 1.51$ A and the y-component at $I = 19.5$ A. From top to bottom: B_{total} is plotted in pink, B_y in black, B_x in blue, B_z in red.

4.1.2. Background compensation

The EMCS can compensate both the x- and y-component of the earth field (see figure 4.2). It has four pairs of coils for each component. To compensate the z-component the two outer air coils of the LFCS were operated additionally (see figure 4.3).

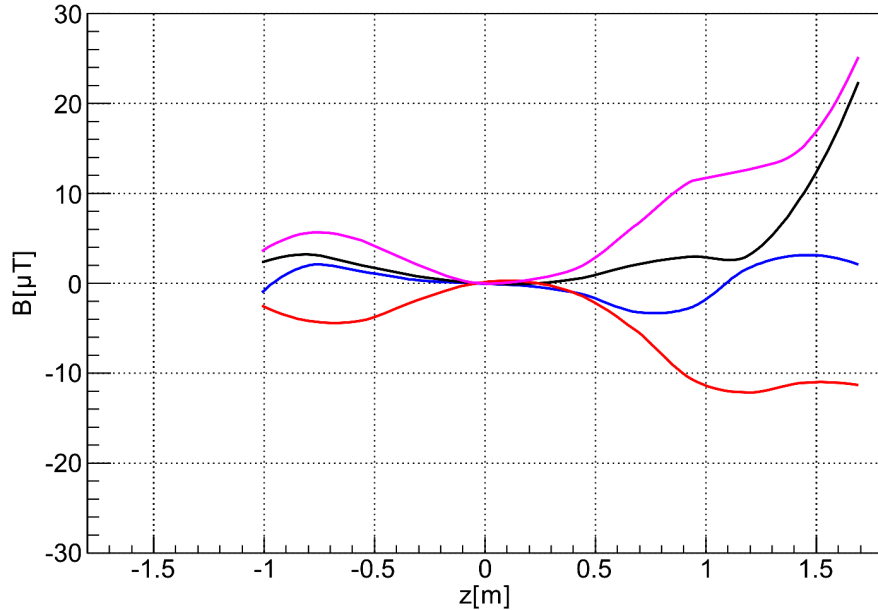


Figure 4.3.: Background compensation with the EMCS and parts of the LFCS Now not only the EMCS (figure 4.2) but also the outer coils of the LFCS are operated. These coils compensated the z-component at $I = 445$ mA. The magnetic field gets bigger as z gets bigger but that is not problematic because the field of the solenoids will be overlying these regions (at $z = 1$ m the field of the solenoids will be about 5 mT). From top to bottom: B_{total} is plotted in pink, B_y in black, B_x in blue, B_z in red.

4.1.3. Magnetic field measurements with the LFCS

The LFCS system consists of three electric circuits which are connected to four air coils. There is an inner air coil and an outer middle air coil at $z = 0$ m. The two outer air coils at $z = \pm 0,5$ m are connected in series and cannot be controlled separately. The three circuits were operated separately at different currents while the resulting magnetic field was measured. Afterwards the values were compared to the theoretical values calculated with Biot-Savart's law (see table 4.1). The resulting maximum difference of about 4% can be tolerated.

Subsequently the whole LFCS was operated together with the EMCS (figure 4.4). The z-component was as expected at $-800 \mu\text{T}$, while the other components were smaller than $20 \mu\text{T}$. However, the x- and y-components had a peculiar shape and generated a background field of $10 \mu\text{T}$ in the analyzing plane. This would mean they cause an error of 3% in the analyzing plane. Hence a simulation was performed to figure out the reasons for this deviation.

Table 4.1.: Comparison of the theoretical and experimental value of the LFCS coils The values in brackets were measurements and calculations with the same air coils at a different current. The values differ by 4% at most, so it is possible to calculate the magnetic field inside the spectrometer with Biot-Savart without measuring.

	theoretical value (Biot-Savart) in μT	experimental value in μT	experimental/ theoretical value
inner air coil at $I=15\text{ A}$	1120	1100	98 %
middle outer air coil at $I=8.8\text{ (18) A}$	308 (629)	300 (600)	97 %
outer air coils at $I=9\text{ (18) A}$	386 (770)	400 (800)	96%

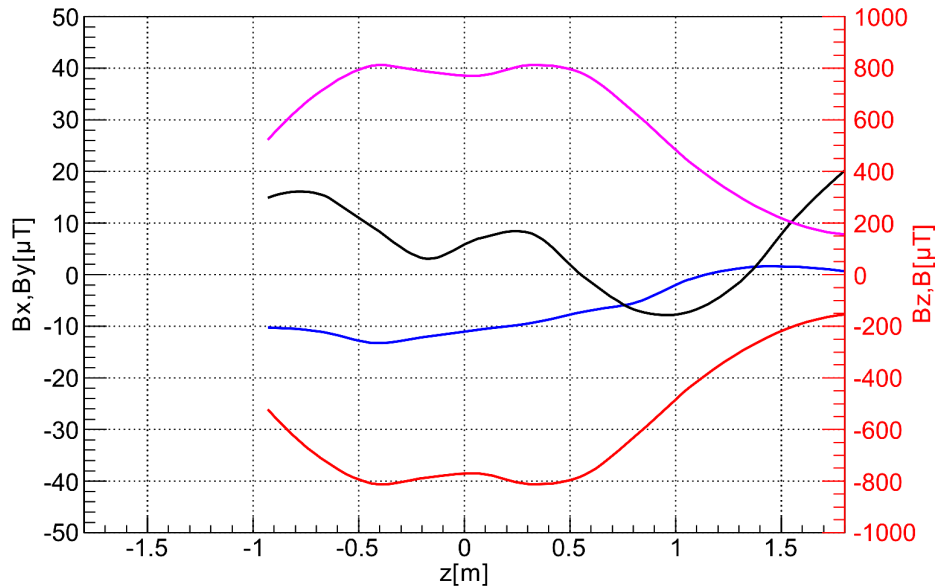


Figure 4.4.: LFCS and EMCS are operating simultaneously. The horizontal EMCS is operated at $I = 1.51\text{ A}$, the vertical at $I = 19.5\text{ A}$. The LFCS is operated as in the Mainz-06 configuration (inner air coil at 5 A , middle outer air coil at 8.8 A , outer air coils at 18 A). B_x (blue) and B_y (black) are plotted on the left axis, B_z (red) and B_{total} (pink) on the right one.

4.2. Comparison to magnetic field simulation

As the magnetic field measurements showed equivocalities in the x- and y-component, specific field calculations were done to explain them. For these simulation the package Kassiopeia was used (field simulation codes used herein are routines by F. Glück [Glü06]). The main idea was to investigate the influence of a skewly installed measurement stack on the magnetic field measurements. The influence should be rather pronounced in the x- and y-component because a skewed sensor would attribute parts of the z-component to the other ones. As the z-component is nearly two orders of

magnitude bigger any small skewness will result in deviations. In figure 4.5 such a calculation is shown. It is evident that the deviation of the x- and y-components can be described sufficiently well with a skewed stack.

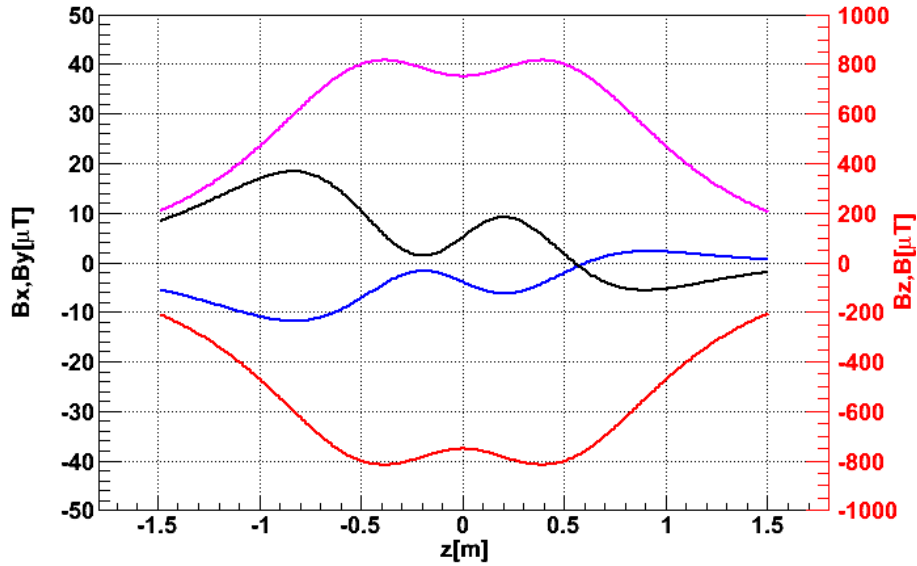


Figure 4.5.: Simulation of the LFCS There were the following parameters in this simulation: The stack is mounted at $x = -0.01$ m and $y = 0.02$ m instead of being at $x = y = 0$ m. The angle to the x-axis is 0.3° and to the y-axis -0.4° . These values are within the mechanical accuracy. The y-component looks just like the measured one; due to unknown reasons the measured x-component is flatter than the simulated one. B_x (blue) and B_y (black) are plotted on the left axis, B_z (red) and B_{total} (pink) on the right one.

4.3. Conclusion

The LFCS and the EMCS are working as expected and operate fine at their designated currents. The maximum difference between the measured and the theoretical values is 4% at most, which is acceptable. The final values for the currents are summarized in table 4.2.

Of course it would have been better to take more care in the positioning of the measurement stack, but a sufficient accuracy would require a major redesign of the positioning system as can be seen by the very small deviations compared to the simulation.

Table 4.2.: Final values for the current of the EMCS and the LFCS

System	Air coil	Current in A
EMCS	horizontal	1.51
	vertical	19.5
LFCS	inner air coil	5
	middle outer air coil	8.8
	outer air coils	18

5. Conclusion and outlook

Neutrino oscillations have revealed that neutrinos have finite non-zero masses. As there are only upper limits on the neutrino mass up to now, it is important for particle physics and cosmology to determine their absolute mass scale.

The KATRIN experiment is currently being set up at KIT with the aim to determine the "electron neutrino mass" with a sensitivity of 200 meV (90 % C.L.) by analysing a narrow region close to the endpoint of the tritium β -spectrum by a MAC-E-Filter with unprecedented precision. A significant issue for the long-term tritium scanning are small variations of the high retarding voltage of this filter, which have to be monitored by the monitor spectrometer.

Within this diploma work the monitor spectrometer was installed and partly commissioned. The vacuum system was overhauled and commissioned successfully. The heating, high voltage and magnetic systems were installed and thoroughly tested. For the source part several options were tested in the past years which have resulted in the option of a solid state $^{83}\text{Rb}/^{83\text{m}}\text{Kr}$ source as the most promising method to achieve a highly stable β -emitter. As the detector was not finished during the time frame of this work the overall system could not be commissioned.

The air coil system consisting of the EMCS and the LFCS was tested successfully. The EMCS was installed and now allows to compensate the earth field background in the analysing plane properly. The magnetic field generated by the LFCS is as expected. Within this work the final input parameters for the air coil system were determined with high accuracy.

In the scope of this work also the data analysis software was prepared and tested and validated with previous data from Mainz. The preliminary slow control and the data acquisition are ready for first measurements and the controlling system PCS7 will be finished soon.

Altogether the monitor spectrometer is ready for measurements by the time the

detector is installed. In the appendix a newly installed wire scanner is described, as well as a measurement programme for the commissioning.

Appendix

A. The wire scanner

A newly designed wire scanner has been installed at the monitor spectrometer at the flange between the source and the spectrometer tank. The blades of the scanner can be moved into the beam and stop the electrons in a particular section of the flux tube. It can be used for scanning of the beam profile and for cleaning of Penning traps.

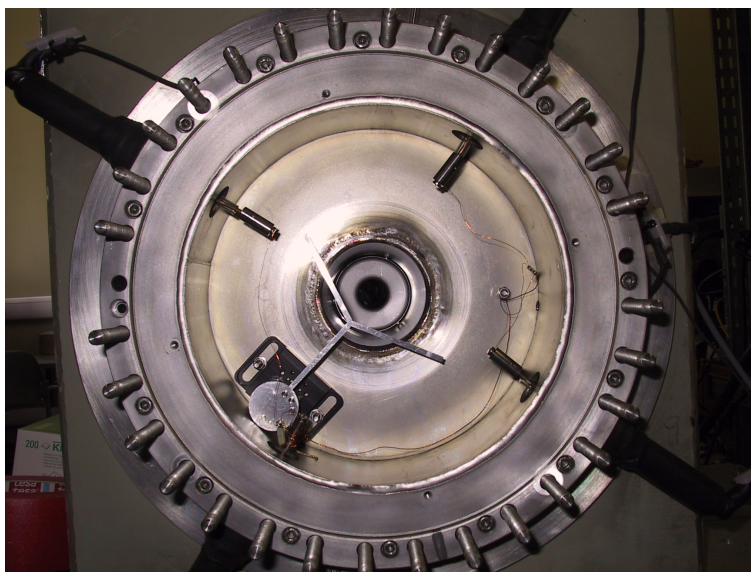


Figure A.1.: The wire scanner at the monitor spectrometer. As it is installed directly in the high field region of the solenoid, a piezo rotator was used. On top of it the wire scanner is mounted. In this position the beam line is unperturbed. The cables are guided outside through the insulators, which were already installed.

Scanning of the beam profile will be possible as the design of the scanner allows to scan the beam both horizontally and vertically (see figure A.1).

Figure A.2 shows an expected spectrum with the wire scanner. When the wire scanner enters the flux tube the count rate decreases. After the scan of the first blade the count rate has its normal level until the second one enters.

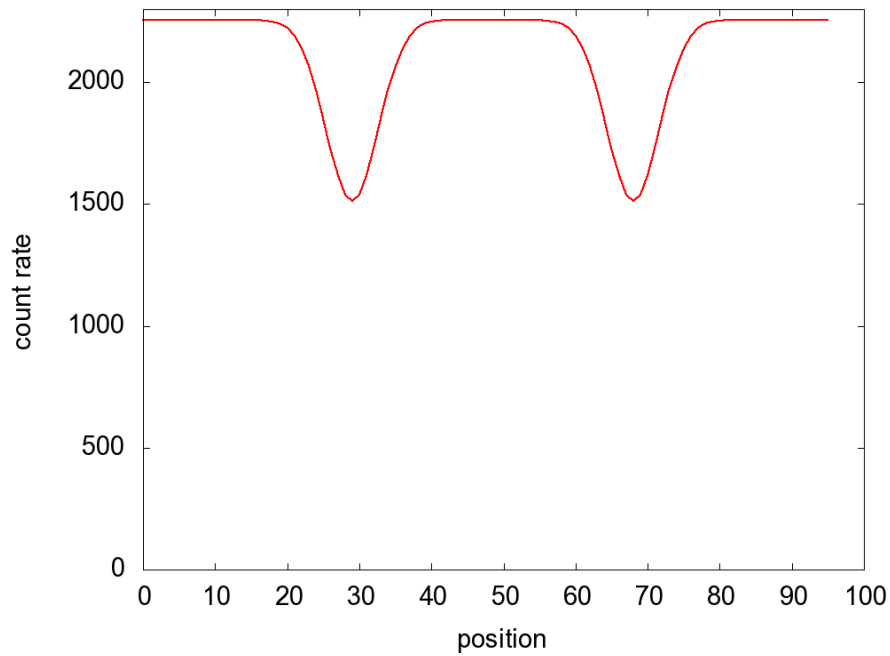


Figure A.2.: An expected spectrum with the wire scanner For this purpose the fluxtube was assumed to be gaussian. Then the sum of all the calculated values of the gaussian distribution but the ones covered by the respective scanner blade were calculated for each position of the scanner.

This spectrum has to be analysed by a two dimensional distribution because it is influenced by two effects: The areas that are covered by the scanner blade change in their size and the flux tube intensity varies during the scan of a blade.

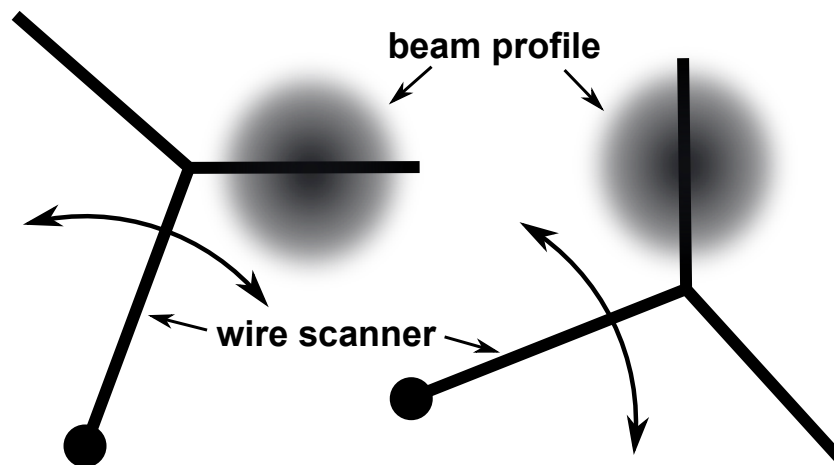


Figure A.3.: Wire scanner scanning the flux tube The big arrows show the possible scan directions. The sketch on the right side illustrates the horizontal scan; the left side the vertical. It can be seen that the area which is covered by the scanner blade changes as well as the intensity of the flux tube. Hence the distribution has to be two dimensional.

Cleaning Penning traps was already tested for the KATRIN setup with different kinds of wire scanners (see [BVB⁺10] for example). A Penning trap is the confinement of electrons by an electrostatic potential in axial direction and a magnetic field in radial direction. At the KATRIN experiment there are several potential Penning traps where the stored electrons can cause background by ionising residual gas. Although Penning traps will not be an issue at the monitor spectrometer because of its high count rates, the wire scanner allows to analyze this effect in a profound way.

B. Radon measurements and simulations

In the ongoing preparations for the main spectrometer commissioning measurement, all materials used in places where traces of radioactivity might be critical were screened by γ -spectroscopy. It turned out that the zirconium vanadium alloy used in the NEG getter pumps contains traces of protactinium including its respective daughters.

Therefore the actinium series (i.e. decay chain of ^{235}U) had to be investigated in more detail (figure B.4). Within this decay chain ^{219}Rn is produced which has a half life of 4s. Hence it can decay in the spectrometer volume if it is emanated with thermal energies from a surface inside the spectrometer. After the decay shake-off, Auger, Coster-Kronig and conversion electrons are set free. These secondaries can be trapped inside the spectrometer volume and create further electrons by elastic scattering, inelastic scattering and ionization of residual gas molecules, which cause the observed background (for more details see [Frä10]).

One possible source for ^{235}U were the NEG getter strips from SAES. The following chapter B.1 describes measurements with the getter material and chapter B.2 presents simulations on how radon ions emanate from the getter.

Parent+Daughters	Half-life	Branching Ratio	Decay	N(atoms)	A(Bq)
92 U235	7.0E8 y	1; 7.20E-11; 8.00E-12; 8.00E-12; 8.00E-12	α ; SF; Ne20; Ne25; Mg28	3.2E+19	999
90 Th231	1.06 d	1; 4.00E-13	β^- ; α	1.3E+08	999
91 Pa231	3.3E4 y	1; 1.34E-11; 3.00E-12; 9.90E-15	α ; Ne24; SF; F23	1.5E+15	999
89 Ac227	21.79 y	0.9862; 1.38E-02	β^- ; α	9.9E+11	999
90 Th227	18.72 d	1	α	2.3E+09	985
88 Ra223	11.43 d	1; 8.90E-10	α ; C14	1.4E+09	999
86 Rn219	3.96 s	1	α	5.7E+03	999
84 Po215	1.78 ms	1; 4.00E-06	α ; β^-	2.6E+00	999
82 Pb211	36.1 m	1	β^-	3.1E+06	999
83 Bi211	2.17 m	0.99727; 2.73E-03	α ; β^-	1.9E+05	999
81 Tl207	4.77 m	1	β^-	4.1E+05	996
82 Pb207 Stable	stable			3.0E+16	0
87 Fr223	21.8 m	0.99994; 6.00E-05	β^- ; α	2.6E+04	14
2 He4 Stable	stable			0	0

Figure B.4.: Actinium series Decay chain of ^{235}U . [Frä10]

Parent+Daughters	Half-life	Branching Ratio	Decay	N(atoms)	A(Bq)
90 Th232	1.4E10 y	1; 1.00E-05; 1.40E-11; 2.78E-12; 2.78E-12	α ; β^- ; β^- ; SF; Ne24/Ne26; Ne26	6.4E+20	1000.0
88 Ra228	5.75 y	1	β^-	2.6E+11	1000.0
89 Ac228	6.15 h	1	β^-	3.2E+07	1000.0
90 Th228	1.91 y	1; 1.13E-13	α ; O20	8.7E+10	1000.0
88 Ra224	3.64 d	1; 4.00E-11	α ; C14	4.5E+08	1000.0
86 Rn220	55.8 s	1; 1.00E-05	α ; β^- ; β^-	8.0E+04	1000.0
84 Po216	150 ms	1; 1.00E-05	α ; β^- ; β^-	2.2E+02	1000.0
82 Pb212	10.64 h	1	β^-	5.5E+07	1000.0
83 Bi212	1.01 h	0.64056; 3.59E-01; 1.40E-04	β^- ; α ; β^- ; α	5.2E+06	1000.0
84 Po212	298 ns	1	α	0.0E+00	0.0
82 Pb208 Stable	stable			3.2E+16	0.0
81 Tl208	3.05 m	1	β^-	9.5E+04	359.3
2 He4 Stable	stable			0.0E+00	0.0

Figure B.5.: Thorium series Decay chain of ^{232}Th . [Frä10]

B.1. Radon measurements in Mainz

For these measurements a container with getter material was connected to the Mainz spectrometer. To calibrate this setup a known radon source (^{232}Th) was put in a separat container that could be disconnected from the spectrometer. This thorium source is based on a piece of cotton fabric, impregnated with a thorium salt and commercially available as gas mantle. The decay chain of ^{232}Th is shown in figure B.5 on the right; here ^{220}Rn is the isotope that causes background.

The signatures of radon-decay can be seen both in the total rate in a specific energy window and by bunches of events (so-called multiple events are detected). These bunches should be enhanced by an elevated pressure, as there are more atoms to scatter with. Accordingly, for these measurements the pressure was increased to a few times 10^{-8} mbar.

The results are shown in figure B.6. The total count rate was 18% higher than without the getter and the number of bunches (in this case each event that had three or more counts at the same time was counted as a bunch) was 27% higher. The rates with thorium and the getter pump were four (total rate) and eight (number of bunches) times higher, indicating thereby that the measurement method worked.

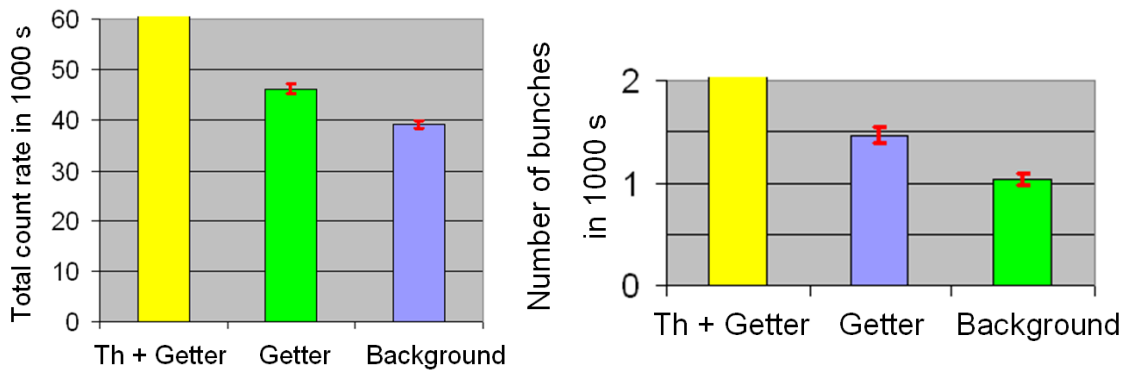


Figure B.6.: Measurements of the total rate and the number of bunches in 1000 s without getter, with getter and with getter and thorium. The measurements with the getter show an increase of the rate (18%) and the number of bunches (27%). The columns of thorium and the getter are cutted as they are four (total rate) and eight (number of bunches) times higher than the ones with only getter. These charts show the average of several measurements. [Sch05]

The activity of the getter strips was determined to be $A = 5$ Bq. In 1000 s there were seven counts due to ^{219}Rn decay, so the detection efficiency was 0.14%. The detection efficiency of ^{220}Rn was 0.57% in these measurements. Now it has to be considered that for ^{220}Rn it might be much easier to get into the spectrometer volume, while ^{219}Rn first has to leave the getter strips (most of the ions were stuck in the getter; see next chapter). On the other hand, ^{220}Rn has a longer half-life (56 s) than ^{219}Rn (4 s), so some of the ^{220}Rn ions do not decay in the spectrometer volume, but are pumped out before they decay.

In summary it seems to be certain by the analysis of these measurements alone that the NEG getter strips are causing background with ^{219}Rn .

B.2. Radon simulations

Positively charged ions are generated by α -decay with a typical recoil energy of several keV. Although the half life of ^{219}Rn is only 4 s, they will impinge much earlier a wall with these energies and do not cause background. The implication is that only neutralized radon atoms with thermal energies can generate secondary electrons and cause background.

In the following it will be described in detail how much ^{219}Rn ions can get into the spectrometer volume and which energies they have. At first, the starting energy of the ^{219}Rn ions is determined, then the simulations with the programme SRIM [Zie10] are presented and the emanation of the ions from the surface is described.

First an estimate of the **starting energy of ^{219}Rn** is needed. The mother isotope of ^{219}Rn is ^{223}Ra . ^{223}Ra decays to 100 % through α decay. The distribution of the α energies is shown in figure B.7. These energies are located in a relatively small range, so it is justified to use the weighted average as the energy of the α . That made it straightforward to calculate the starting energy of the ^{219}Rn ions based on the kinematics of a two body decay. This yields a kinetic energy $E = 103$ keV.

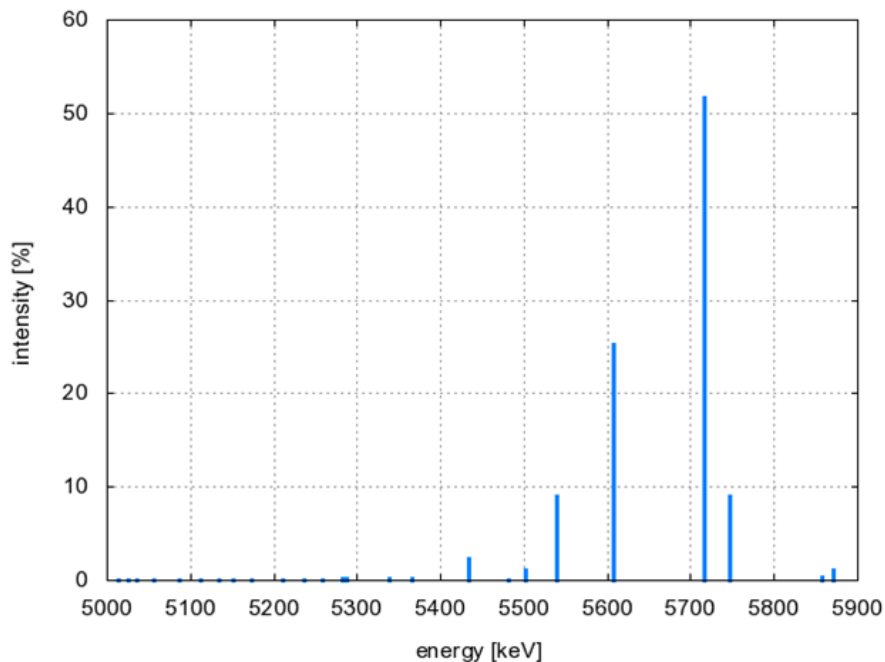


Figure B.7.: Distribution of alpha energies at the decay of ^{223}Ra . As they are close together the weighted average $E_\alpha = 5666$ keV was used.

The programme **SRIM** was then used to simulate the explanation and implantation of ions in matter. The intention was to get an idea of the number of ions that are explanted due to their energy after the α decay of ^{223}Ra .

The programme SRIM uses the ion type, the starting energy, the starting angle and the starting material to get a distribution of the ions in the material. It also gives the energy and angle distribution of the explanted ions.

The general procedure is shown in figure B.8.

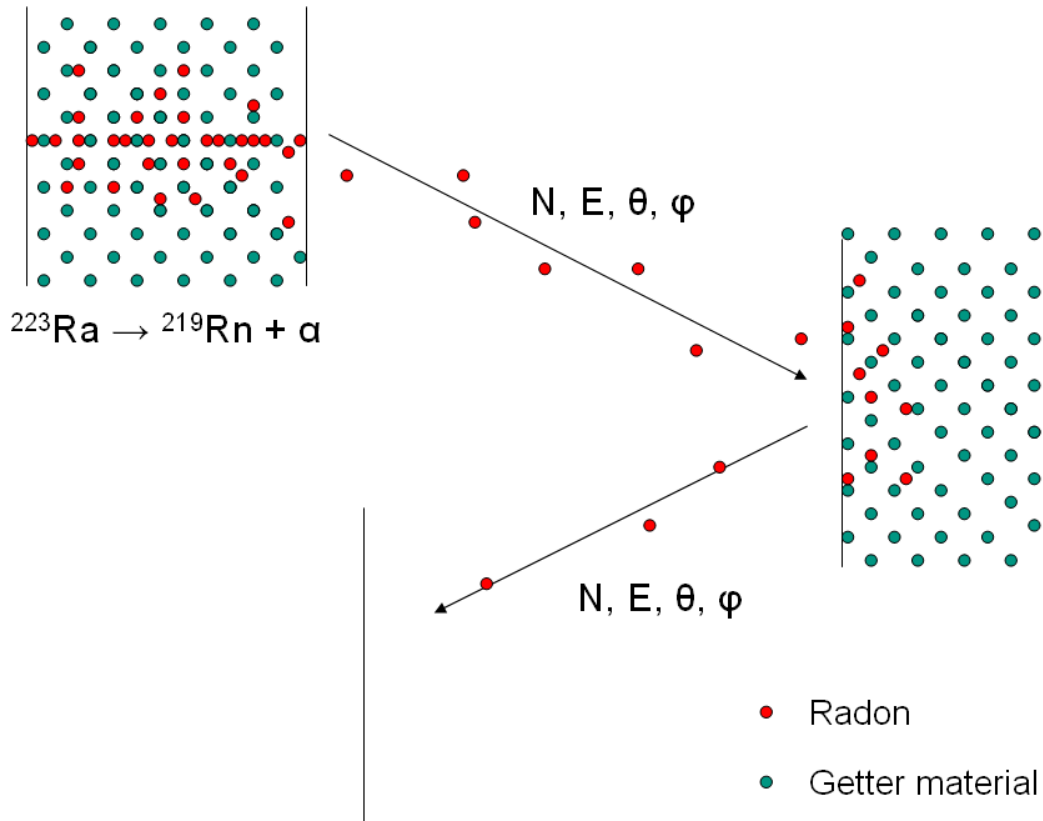


Figure B.8.: Procedure of the SRIM simulations In the upper left the mother isotope ^{223}Ra decays into ^{219}Rn . Some of these ions are explanted with specific angles and energies. These parameters will be determined by SRIM and used as starting parameters for the implantation into the next surface they hit (right side of the sketch). Some of the ions are not implanted but backscattered - for them the same procedure begins again.

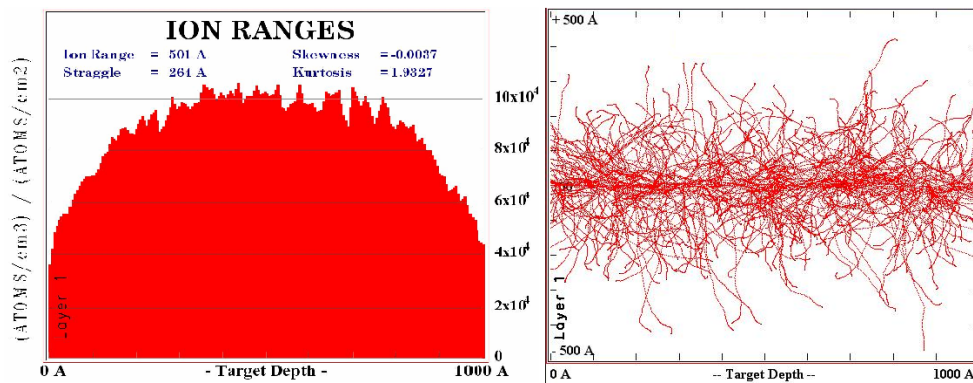


Figure B.9.: Explantation simulation by SRIM ^{219}Rn ions start in the NEG getter material with $E = 103 \text{ keV}$. *Left:* Ion distribution in the getter material with 10^5 ^{219}Rn ions. The drop at the outer parts is caused by the explanted ions. *Right:* Ion trajectories in the xz-plane shortly after the start of the simulation.

The starting material of the simulation is the NEG getter material. It consists of 70 % zirconium, 24.6 % vanadium and 5.4 % iron. For the depth of the getter material a value of 100 nm was used, which is the maximum range of ions in the getter material

with a start energy of 103 keV. The simulation started with 10^5 single ^{219}Rn ions with an energy of 103 keV, each path starting with a random angle and depth (the depth is the z-axis). Without loss of generality x and y were set to zero. The resulting distribution of the ions in the getter material can be seen in figure B.9. A fraction of 5.7% of the started ions were explanted with an average energy of 45 keV.

Looking back at figure B.8 the next step is the implantation on the right side. Therefore the explanted ions from the explantation are implanted into the adjacent getter layer which can be seen in figure B.10. Now, a fraction of 3.7% of the implanted ions are scattered back with an average energy of 10 keV. As these correspond to only 0.21% of the primary yield of explanted ions they are neglected.

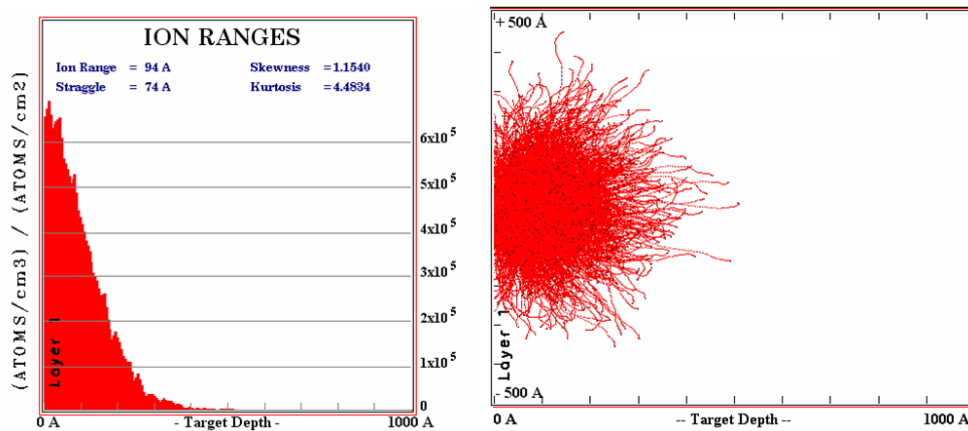


Figure B.10.: Implantation simulation by SRIM ^{219}Rn ions are implanted into getter material with an average energy of 45 keV. *Left:* Ion distribution: The ions stay close to the surface. *Right:* Ion trajectories in the xz plane.

Following these simulations one can state that about 6% of the started ^{219}Rn ions are outside the getter. But these ions typically have too high energies to decay inside the tank volume. So the idea was that the ions that stayed close to the surface could emanate with very small kinetic energies.

This **emanation** process was already investigated with ^{83}Rb ($^{83\text{m}}\text{Kr}$) implanted into gold and platinum (for detail see [Zbo10]). In this case one also deals with a noble gas atom contained in a metal and therefore the analogy should be justified. As noted earlier, ^{83}Rb was implanted into gold or platinum and subsequently decayed into $^{83\text{m}}\text{Kr}$ (see chapter 3.7.4.2). These investigations have given the result that up to 11% of the krypton gas emanated out of the substrate. Now the specific question was about the depth to which these 11% were implanted into the metal. Therefore another SRIM simulation was done (see figure B.11), where ^{83}Rb was implanted into gold. The outer 11% are located in the outer seven atomic layers which corresponds to 2.1 nm.

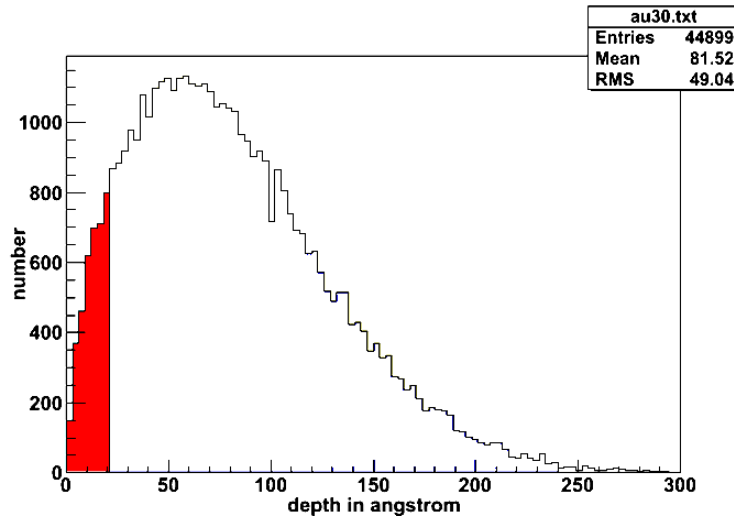


Figure B.11.: Implantation simulation by SRIM Here ^{83}Rb was implanted into gold. The single columns represent one atomic layer (about 3 \AA). The 11 % that emanate are indicated by the red area and correspond to a depth of penetration of 7 atomic layers ($2.1 \text{ nm} = 21 \text{ \AA}$).

To complete the analogy, the percentage of the Radon ions that are in the outer seven atomic layers of the getter material has to be determined. For each part of the simulation (explantation and implantation) that are about 1 % of the started ions (see figure B.12).

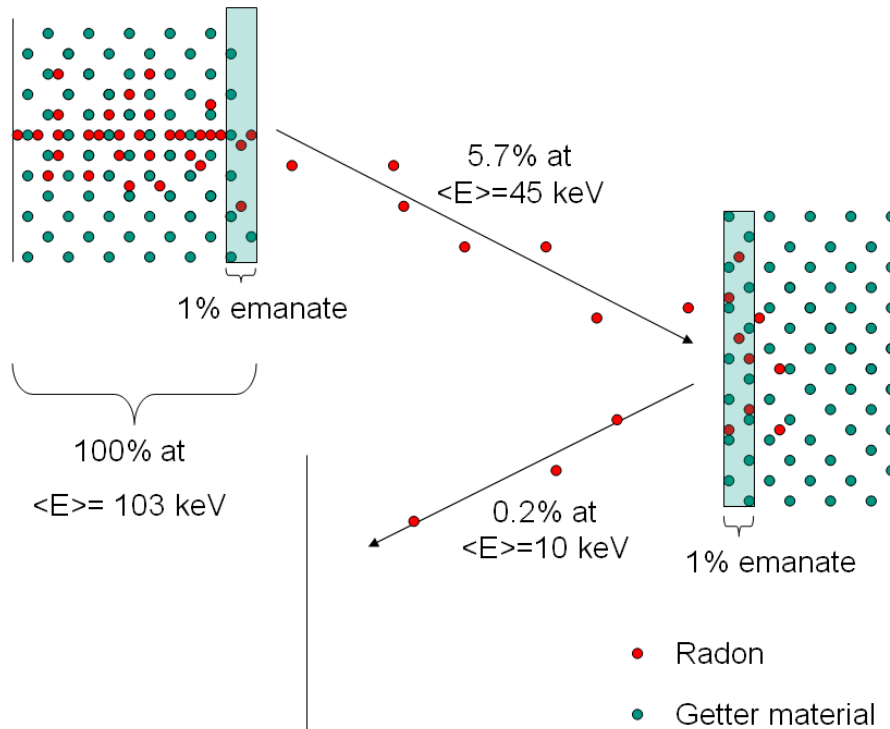


Figure B.12.: Results of the SRIM-simulations and emanating ions 2 % of the radon ions get out of the getter with thermal energies.

Altogether 2 % of the radon ions that were generated in the getter layer thus emanate into the spectrometer volume. But up to now only the outer 100 nm of the

getter material were regarded.

So it is important to know to what extent the outer 100 nm contribute in mass in respect to the whole getter volume. The assumption made here was that the getter material consists of uniformly sized spheres - with $1 \text{ m}^2/\text{g}$ (value from SAES) a grain size of $0.922 \mu\text{m}$ can be deduced. Hence the outer 100 nm correspond to 30 % of the getter volume.

In summing up one can state that altogether 0.7 % of the generated radon ions emanate into the spectrometer volume as neutral gas atoms.

This result is consistent with the measurements and investigations done in [Frä10] for the pre-spectrometer and the previously presented ones in Mainz. At the pre-spectrometer, the activity of ^{223}Ra was determined to be 8 Bq which leads to a detection efficiency of about 0.1 %. This is consistent with the one determined in Mainz (0.14%).

B.3. Conclusion

This chapter has further strengthened the case that the NEG getter strips are a probable cause for the background in Mainz.

In the course of the radon measurements, the rate and the number of bunches clearly was increased by the getter strips. The simulations and the analogy to krypton have explained how the radon can decay inside the spectrometer.

So the 3 km of NEG getters are a serious source for the background at KATRIN. In the meantime further investigations on this problem have been presented in [Frä10] and [Gör10].

C. Detector commissioning

In the final days of this work the detector unit was delivered and initial tests at room temperature were performed. It should be emphasized that for normal operation the detector should be cooled with liquid nitrogen.

For these measurements, a ^{241}Am photon source was put in front of the detector. The resulting spectrum can be seen in figure C.13.

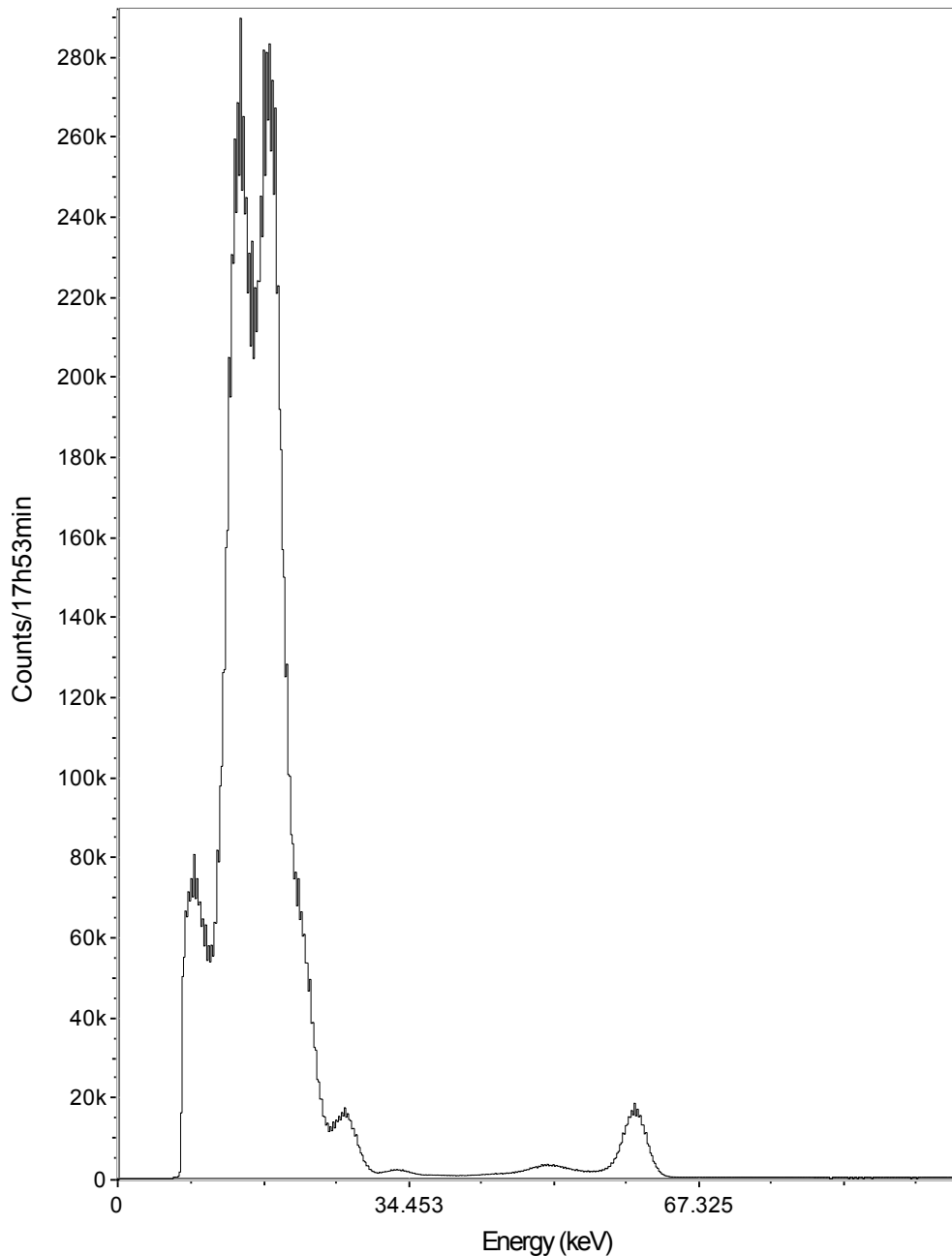


Figure C.13.: Americium spectrum measured with the monitor spectrometer detector. Five peaks can be seen at 9 keV, 14 keV, 18 keV, 26 keV and at 60 keV.

Figure C.14 shows a ^{241}Am spectrum with higher resolution that was measured in [LDM94]. It is consistent with the spectrum from the new detector at the monitor beamline: the X-ray and γ -ray lines can be seen clearly. Only the peak at 9 keV cannot be allocated and thus can be attributed to electronic noise.

The spectrum in figure C.13 was measured by one of the five detector elements (see figure 3.18). The other ones showed also the same characteristics of the spectrum, however, there was much more noise, which should not be a problem once the detector is cooled.

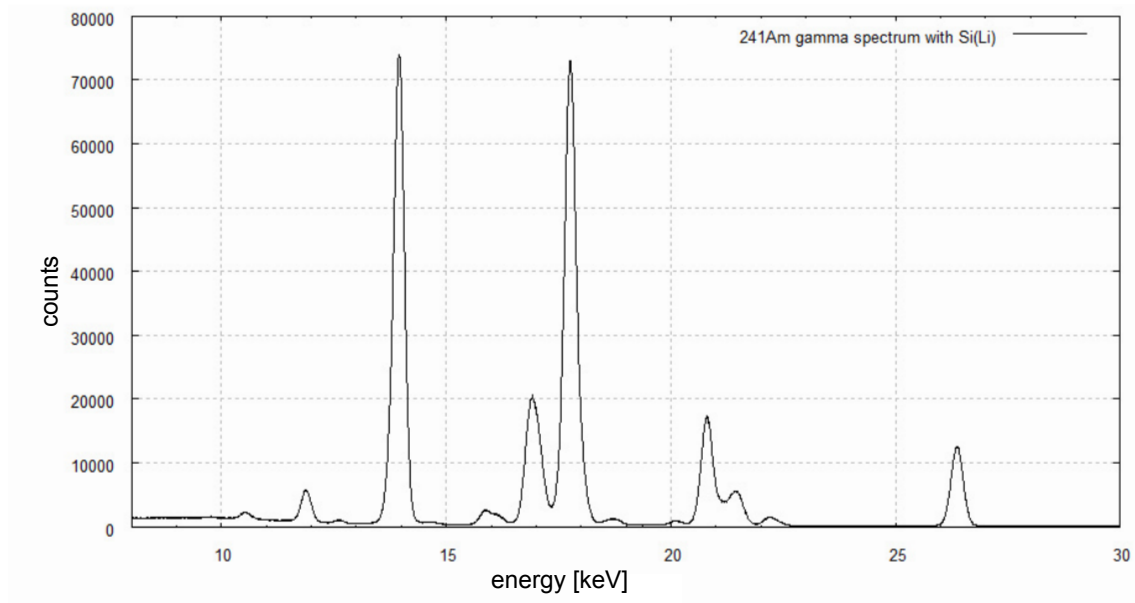


Figure C.14.: Americium spectrum Here the characteristic lines can be seen with high resolution. The two dominant peaks are X-ray lines at 13.9 keV and 18 keV. The γ -ray line at 26.3 keV can also be seen. This plot ends at 30 keV, so that the 59.5 keV γ -ray line is not displayed. [LDM94]

D. Measurement programme

In this chapter a preliminary schedule of the final commissioning and the first measurements will be presented.

The commissioning of the monitor spectrometer will be finished at the end of 2010. In December 2010 the first complete spectrum of krypton should be measured. At that time the final high voltage setup is not yet installed so this will basically be a technical test. The resulting lines (KLMN for the 32 keV transition and LMN for 9.4 keV) can however be analysed with regard to energy resolution and loss of electrons.

In 2011 several long-term measurements are mandatory. The most important one will be the analysis of the long-term stability of the K and L lines of the 32 keV transition. Additionally, there will be specific studies of the transmission losses, of possible satellites in the vicinity of the lines and an investigation of the doublet structure of the N-32 line. These measurements will last about three months.

Another important study will be the investigation of the storage of electrons in the monitor spectrometer. Therefore, stored electrons from krypton or radon decays will be analyzed. This again will take several months.

It is vital for the production of implanted rubidium sources to establish a supply in addition to ISOLDE. Our collaboration partners in Bonn have already made some tests with stable Rb-beams. Of particular interest is the development of a table top implanter without mass separation. Although it is not obvious that unseparated samples are useful, tests with evaporated sources have allowed to measure conversion electrons from $^{83\text{m}}\text{Kr}$.

New monitoring sources should be made in spring 2011. The search for new substrates and alternative source production methods should go on in parallel.

Apart from that, the monitor spectrometer should also measure the stability of the K-32 and L-32 lines over a couple of months. In the course of these investigations the high voltage concept, which is based on the simultaneous operation of the main and monitor spectrometer with the same power supply, should be implemented and thoroughly be tested to minimize the errors of the KATRIN neutrino mass measurements.

List of Figures

1.1.	Neutrino sources	3
1.2.	Results of the Super-Kamiokande experiment	4
1.3.	Results from SNO and Super-Kamiokande experiments	5
1.4.	Summary of measured oscillation parameters	6
1.5.	Neutrino mass eigenstates m_i as a function of the lightest eigenstate m_1	7
1.6.	Constituents of the energy density of the universe	7
1.7.	Energy spectrum of electrons at the tritium-decay	9
2.1.	Principle of the MAC-E-Filter	14
2.2.	Transmission function	15
2.3.	The KATRIN experiment	16
2.4.	Simulation of one year KATRIN measurements	18
3.1.	Monitor spectrometer	21
3.2.	Cylinder- and wire electrode	22
3.3.	Magnetic field configuration for the Mainz-06 setup	22
3.4.	Vacuum pumps at the monitor spectrometer	23
3.5.	Pressure sensors of the vacuum system	24
3.6.	Pressure development over several weeks	25
3.7.	Magnetic field line contour	26
3.8.	The source part of the monitor spectrometer	27
3.9.	Sourceholder	28
3.10.	Magnetic field simulation at the source	28
3.11.	Influence of the work function	29
3.12.	Integrated spectrum of the Am/Co source	30
3.13.	Decay scheme of rubidium	30
3.14.	Results from the CKrS in Mainz	32
3.15.	Setup at ISOLDE facility	33
3.16.	Long-term stability of SKrS sources	33
3.17.	Magnetic field simulation at the detector side	34
3.18.	Old and new detector	35
3.19.	Spectra of the K-32 conversion electrons	36
3.20.	Dead time correction	37
3.21.	Integrated spectrum	38
4.1.	Magnetic field background	40
4.2.	Background compensation with the EMCS	40
4.3.	Background compensation with the EMCS and parts of the LFCS	41

4.4. LFCS and EMCS	42
4.5. Simulation of the LFCS	43
A.1. The wire scanner	47
A.2. An expected spectrum with the wire scanner	48
A.3. Wire scanner scanning the flux tube	48
B.4. Actinium series	50
B.5. Thorium series	50
B.6. Measurements of the total rate and the number of bunches in 1000 s .	51
B.7. Distribution of alpha energies	52
B.8. Procedure of the SRIM simulations	53
B.9. Explantation simulation by SRIM	53
B.10. Implantation simulation by SRIM	54
B.11. Implantation simulation by SRIM	55
B.12. Results of the SRIM-simulations and emanating ions	55
C.13. Americium spectrum	57
C.14. Americium spectrum	58

List of Tables

3.1. Conversion electron energy of the 32 keV transition	31
4.1. Comparison of theoretical and experimental values of the LFCS coils	42
4.2. Final values for the current of the EMCS and the LFCS	43

Bibliography

- [A⁺08a] C. Amsler *et al.*: *Review of Particle Physics*. Physics Letters B, 667(1-5):1 – 6, 2008, ISSN 0370-2693. <http://www.sciencedirect.com/science/article/B6TVN-4T4VKPY-2/2/2fe3ceb40a4d144f48321db99160ecb2>, Review of Particle Physics.
- [A⁺08b] C. Arpesella *et al.*: *First real time detection of ${}^7\text{Be}$ solar neutrinos by Borexino*. Physics Letters B, 658(4):101 – 108, 2008, ISSN 0370-2693. <http://www.sciencedirect.com/science/article/B6TVN-4PTW4KP-1/2/b05ac0237a29b0a7da944b6ba452882d>.
- [Bor00] B. Bornschein: *Untersuchung systematischer Effekte und erste Tritiummessungen mit dem verbesserten Mainzer Neutrinomassenexperiment*. Dissertation, Johannes Gutenberg-Universität Mainz, 2000.
- [Bru06] Jürgen Brunner: *ANTARES - Astronomie in der Tiefsee*. Sterne und Welt- raum, Mai 2006. <http://www.astronomie-heute.de/artikel/835876>.
- [BVB⁺10] Beck, M., Valerius, K., Bonn, J., Essig, K., Glück, F., Ortjohann, H.-W., Ostrick, B., Otten, E.W., Thümmeler, Th., Zboril, M. und Weinheimer, C.: *Effect of a sweeping conductive wire on electrons stored in a Penning-like trap between the KATRIN spectrometers*. Eur. Phys. J. A, 44(3):499–511, 2010. <http://dx.doi.org/10.1140/epja/i2010-10959-1>.
- [C⁺56] C. L. Cowan *et al.*: *Detection of the Free Neutrino: a Confirmation*. Science., 88:103–104, 1956.
- [Col01] SNO Collaboration: *Measurement of the Rate of $\nu_e + d \rightarrow p + p + e^-$ Interactions Produced by ${}^8\text{B}$ Solar Neutrinos at the Sudbury Neutrino Observatory*. Phys. Rev. Lett., 87(7):071301, Jul 2001.
- [Col05] KamLAND Collaboration: *Measurement of Neutrino Oscillation with KamLAND: Evidence of Spectral Distortion*. Phys. Rev. Lett., 94(8):081801, Mar 2005.
- [Col08] SNO Collaboration: *Independent Measurement of the Total Active ${}^8\text{B}$ Solar Neutrino Flux Using an Array of ${}^3\text{He}$ Proportional Counters at the Sudbury Neutrino Observatory*. Phys. Rev. Lett., 101(11):111301, Sep 2008.
- [D⁺62] G. Danby *et al.*: *Observation of High-Energy Neutrino Reactions and the Existence of Two Kinds of Neutrinos*. Phys. Rev. Lett., 9(1):36–44, Jul 1962.
- [Dav55] Raymond Davis: *Attempt to Detect the Antineutrinos from a Nuclear Re- actor by the ${}^{137}\text{C} (\bar{\nu}_e, e^-) {}^{37}\text{A}$ Reaction*. Phys. Rev., 97(3):766–769, Feb 1955.

- [Fer34] E. Fermi: *An attempt of a theory of beta radiation. 1.* Z. Phys., 88:161–177, 1934.
- [Fla04] B. Flatt: *Voruntersuchungen zu den Spektrometern des KATRIN-Experiments.* Dissertation, Johannes Gutenberg-Universität Mainz, 2004.
- [Frä10] Florian Fränkle: *Background Investigations of the KATRIN Pre-Spectrometer.* Dissertation, KIT, 2010.
- [Glü06] Ferenc Glück: *The 3-dimensional magnetic field calculation program package magfield3,* 2006. <http://fuzzy.fzk.de/bscw/bscw.cgi/d217038/magfield3.pdf>.
- [Gör10] Stefan Görhardt: *Reduktion der durch Radon induzierten Untergrundprozesse in den KATRIN Spektrometern.* Diplomarbeit, KIT, 2010.
- [Han05] Steen Hannestad: *Neutrino mass bounds from cosmology.* Nuclear Physics B - Proceedings Supplements, 145:313 – 318, 2005, ISSN 0920-5632. <http://www.sciencedirect.com/science/article/B6TVD-4G3CBPY-2C/2/a3e4c3334362d0f4e56520ea60e34197>, NOW 2004.
- [K⁺01] K. Kodama *et al.*: *Observation of tau neutrino interactions.* Physics Letters B, 504(3):218 – 224, 2001, ISSN 0370-2693. <http://www.sciencedirect.com/science/article/B6TVN-42NY3K6-15/2/6aade3e03ecc53fcbf8986e79c267b29>.
- [K⁺04] C. Kraus *et al.*: *Latest results of the Mainz Neutrino Mass Experiment.* Eur. Phys. J. C, 33:s805–s807, 2004. <http://dx.doi.org/10.1140/epjcd/s2003-03-902-9>.
- [Kas08] J. Kaspar: *Am/Co photoelectron source for energy scale monitoring of the KATRIN neutrino experiment.* Dissertation, CZECH TECHNICAL UNIVERSITY IN PRAGUE, 2008.
- [KAT05] KATRIN Collaboration: *KATRIN Design Report 2004, FZKA report 7090,* 2005.
- [KBB⁺] C. Kraus, B. Bornschein, L. Bornschein, J. Bonn, B. Flatt, A. Kovalik, B. Ostrick, E. W. Otten, J. P. Schall, Th Thümmeler *et al.*: *Final results from phase II of the Mainz neutrino mass search in tritium beta decay.*
- [KK⁺] H. V. Klapdor-Kleingrothaus *et al.*: *Evidence for neutrinoless double beta decay.*
- [L⁺99] V. M. Lobashev *et al.*: *Direct search for mass of neutrino and anomaly in the tritium beta-spectrum.* Physics Letters B, 460(1-2):227 – 235, 1999, ISSN 0370-2693. <http://www.sciencedirect.com/science/article/B6TVN-3X3KCBX-15/2/9eb209e6f2dad82ada1232d12540dc50>.
- [LDM94] M.C. Lépy, B. Duchemin und J. Morel: *Comparison of experimental and theoretical L X – ray emission probabilities of ²⁴¹Am, ²³⁹Pu and ²⁴⁰Pu.* Nuclear Instruments and Methods in Physics Research Section A: Accelerators, Spectrometers, Detectors and Associated Equipment, 353(1-3):10 – 15, 1994, ISSN 0168-9002. <http://www.sciencedirect.com/science/article/B6TJM-473M960-57/2/adccddf4ef3bfdc6aac21c509aac6aff>.

- [Mül02] Beatrix Müller: *Umbau des Mainzer Neutrinomassensexperiments und Untergrunduntersuchungen im Hinblick auf KATRIN*. Diplomarbeit, Johannes Gutenberg-Universität Mainz, 2002.
- [Mur10] Hitoshi Murayamas, 2010. <http://hitoshi.berkeley.edu/neutrino>.
- [Ost08] B. Ostrick: *Eine kondensierte 83mKr -Kalibrationsquelle für das KATRIN-Experiment*. Dissertation, Westfälische Wilhelmsuniversität Münster, 2008.
- [Pau30] W. Pauli: *Offener Brief an die Gruppe der Radioaktiven bei der Gauvereinstagung zu Tübingen*. 1930.
- [PDG10] K. Nakamura et al. (Particle Data Group), 2010. ISSN 0370-2693. <http://pdg.lbl.gov>.
- [Rei09] Jan Reich: *Magnetfeldmessungen und Designarbeiten für das EMCS Luftspulensystem am KATRIN Hauptspektrometer*. Diplomarbeit, KIT, 2009.
- [Sch97] Norbert Schmitz: *Neutrinophysik*. Teubner Studienbücher, 1997.
- [Sch05] Klaus Schlösser: *Radon background from NEG-strips measured at the Mainz spectrometer*, 2005.
- [SKC98] Super-Kamiokande Collaboration: *Evidence for Oscillation of Atmospheric Neutrinos*. Phys. Rev. Lett., 81(8):1562–1567, Aug 1998.
- [SKC04] Super-Kamiokande Collaboration: *Evidence for an Oscillatory Signature in Atmospheric Neutrino Oscillations*. Phys. Rev. Lett., 93(10):101801, Sep 2004.
- [SKC05] Super-Kamiokande Collaboration: *Measurement of atmospheric neutrino oscillation parameters by Super-Kamiokande I*. Phys. Rev. D, 71(11):112005, Jun 2005.
- [SNO10] SNO: *experiment homepage*, 2010. http://www.sno.phy.queensu.ca/sno/papers/0502021_figs/.
- [Spa08] Antonin Spalek: *Monte Carlo simulations of electron energy losses in $83\text{Rb}/83\text{mKr}$ vacuum evaporated sources*, 2008.
- [Stu10] M Sturm: *Aufbau und Test des Inner-Loop-Systems der Tritiumquelle von KATRIN*. Dissertation, KIT, 2010.
- [Thü07] Thomas Thümmel: *Präzisionsüberwachung und Kalibration der Hochspannung für das KATRIN-Experiment*. Dissertation, Westfälische Wilhelms-Universität Münster, 2007.
- [Wol78] L. Wolfenstein: *Neutrino oscillations in matter*. Phys. Rev. D, 17(9):2369–2374, May 1978.
- [Zbo10] M. Zboril: *Phd Thesis in preparation*, 2010.
- [Zie10] James Ziegler: *SRIM code*, 2010. <http://www.srim.org/>.

Danksagung

Zum Schluss möchte ich noch allen danken, die zum Gelingen dieser Arbeit beigetragen haben. Besonderen Dank geht an alle Personen der nachfolgenden und sicherlich unvollständigen Liste. Danke,

- Prof. Dr. Guido Drexlin für die interessante und anspruchsvolle Aufgabenstellung und seine Astroteilchenphysik Vorlesungen,
- Prof. Dr. Thomas Müller für die Übernahme der Zweitkorrektur,
- Dr. Klaus Schlösser für die Betreuung, den persönlichen Einsatz und den freundschaftlichen Umgang,
- Martin Babutzka, Pascal Renschler und Benjamin Leiber für ihre Hilfe bei Softwareproblemen,
- Dr. Sascha Wüstling und Lars Petzold für die Entwicklung der Detektorelektronik,
- Achim Wilden, Thomas Höhn und Mitarbeiter für die Installation des PSC7 Systems,
- Bernard Bender, Hendrik Weingardt und Alexey Melechin für die Installationssarbeiten,
- Miroslav Zboril für seine Hilfe bei der Programmierung der Analysesoftware,
- Drahos Venos für die Fertigung der neuen Quellhalter,
- Patrick Pajzer für die slow control Entwicklung,
- Dr. Ferenc Glück für die Beantwortung physikalischer Fragen jeglicher Art,
- Stefan Groh, Alex Windberger, Hendrik Schilling und Jan Hergenhan für das Dart-Projekt,
- Johannes Schwarz, Jan Reich, Robin Gröble, Nancy Wandkowsky, Tobias Bode, Susanne Mertens, Dr. Thomas Thümmeler, Dr. Joachim Wolf, Dr. Udo Schmitt, Dr. Lutz Bornschein, Dr. Jochen Bonn, Armen Beglarian, Luisa Schäfer, Martin Mark und Stefan Görhardt, die alle geholfen haben, meine Zeit während der Diplomarbeit angenehm und produktiv zu machen.

Insbesondere danke ich meinen Eltern und Freunden, die mich während des gesamten Studiums perfekt unterstützt haben.